UNIVERSITY OF TARTU
Faculty of Science and Technology
Institute of Physics

Robert Valner

CHARACTERIZATION OF CUSTOM BUILT SUN SENSORS FOR ESTCube-1

Bachelor's Thesis

Supervisors:

M.Sc. Riho Vendt

M.Sc. Andris Slavinskis

Tartu 2013

Contents

Acronyms and abbreviations

ADC	Analog-to-digital converter
ADCS	Attitude determination and control system
AR	Angular response
CMOS	Complementary metal–oxide–semiconductor
COTS	Commercial off-the-shelf
CVC	Current-to-voltage conversion
E-sail	Electric solar wind sail
FOV	Field of vision
IR	Infrared
LEO	Low-Earth orbit
LSB	Least significant bit
NAI	No albedo influence
PCB	Printed circuit board
PSD	Position sensitive detector
PTA	Position-to-angle
sps	Samples per second
UV	Ultraviolet

1 Introduction

ESTCube-1 is Estonia's first satellite that is developed mainly by the students of University of Tartu [1]. The one-unit satellite is based on CubeSat standard [2]. Its main goal is to test the electric solar wind sail (E-sail) propulsion concept which was proposed by Pekka Janhunen from Finnish Meteorological institute [3, 4]. A 10 m long tether, which is the main payload of the satellite, is used to show the basic proof of concept of E-sail technology. ESTCube-1 was launched into polar Low-Earth Orbit (LEO) where the tether will be reeled out, charged and the effect of ionospheric plasma on the tether will be measured as a change in angular velocity of the satellite [4].

The Attitude Determination and Control System (ADCS), which is a module of ESTCube-1, performs detumbling, pointing and spin control of the satellite and thereby it has a great importance throughout different phases of the mission. The attitude determination system uses three-axis magnetometers, three-axis gyroscopes and two-axis Sun sensors to gather information about the orientation of the satellite in space.

While Commercial Off-The-Shelf (COTS) components are used for magnetometers and gyroscopes, Sun sensors, which determine the orientation of the satellite with respect to the Sun, are custom-built based on analog one-dimensional Position Sensitive Detectors (PSD). Therefore a variety of tests were carried out to characterize and optimize the sensors to operate reliably in conditions confronted in LEO.

Objectives

The main goals of this work are to:

- Optimize,
- Test,
- Calibrate the Sun sensors for the ESTCube-1,
- Evaluate the uncertainty for the attitude measurements of ESTCube-1 with the calibrated Sun sensors.

2 Types of Sun sensors

The wide range of Sun sensor applications has led to the development of numerous sensor types with different Fields of Vision (FOV) values and accuracies. The three basic classes of Sun sensors are *analog sensors*, which have an output signal that is continuous function of the Sun angle; *Sun presence sensors,* which provide a constant output signal whenever the Sun is in the FOV; *digital sensors*, which provide and encoded, discrete output which is a function of the Sun angle. [5]

2.1 Analog Sun sensors

Analog sensors are frequently called cosine detectors because a common type is based on the sinusoidal variation of the output current of a silicon solar cell with Sun angle. The energy deposited in a photocell and, consequently, the output current I is proportional to the cosine of the angle α of incidence of the solar radiation

$$I(\alpha) = I(0) \cdot \cos(\alpha) \tag{2.1}$$

where α is the angle of incidence of light, *I(0)* is max. output current.

A second type of analog sensor uses a bar or mask to shadow a portion of one or more photocells. Different configurations can yield one-axis sensor (Figure 1) or a two-axis sensor (Figure 2) with varying FOVs and resolution. The angle between the normal of the cell surface and the angle of the Sun (angle of incidence) is estimated by comparing the produced photocurrents of respective photocells. [5]

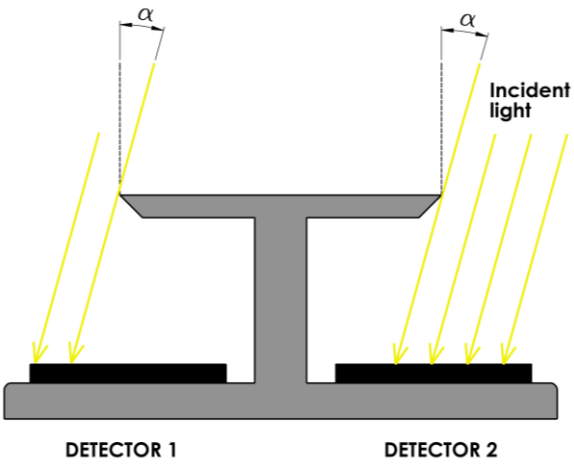

Figure 1. One axis mask Sun sensor where α is the angle of incidence of light. [5]

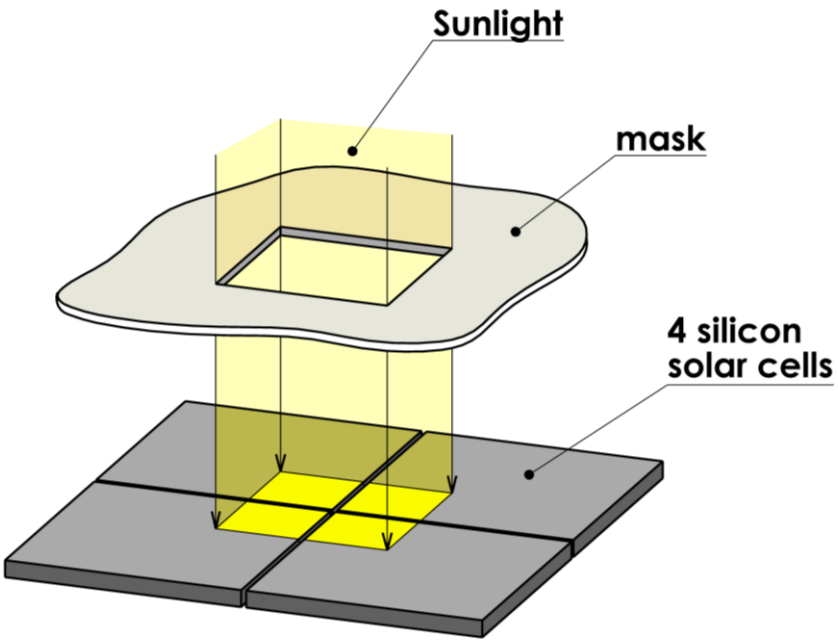

Figure 2. Two axes mask Sun sensor. [5]

2.2 Sun presence sensors

Sun presence detectors are used to protect instrumentation, to activate hardware, and to position the spacecraft or experiments. Sun presence detectors provide a step function response that indicates when the Sun is within the FOV of the detector. [5]

2.3 Digital Sun sensors

Digital Sun sensors produce an encoded discrete output. Typically digital Sun sensors are based on Complementary Metal–Oxide–Semiconductor (CMOS) technology or implementing Gray code system. [6]

The sensors based on the Gray Code (Figure 3) have multiple photocells mounted on a planar surface. Photocells are arranged to form a Gray code system where each cell represents a binary digit. A mask is used to illuminate the photocells and by using an encoding algorithm, position of the projected light can be calculated. [5]

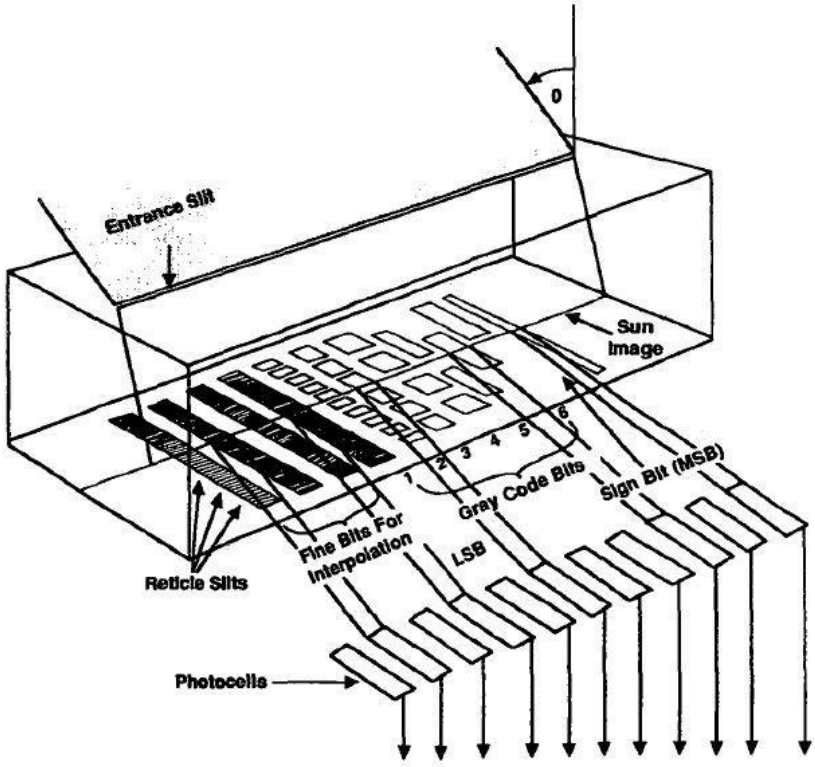

Figure 3. Gray code implemented on digital Sun sensor. [6]

CMOS-based sensors are also known as active pixel sensors. An illustration of the basic layout of a pinhole-based system is shown in Figure 4. The CMOS-based Sun sensor works as a simple pinhole camera, projecting the Sun's image onto a sensor. The image of the Sun is

digitized. The detection of the spot is typically performed by centring process, which sums the intensities in an area of pixels and determines the centroid of intensity. Using geometry and the location of the centroid, the satellite's angle to the Sun can be calculated. [7]

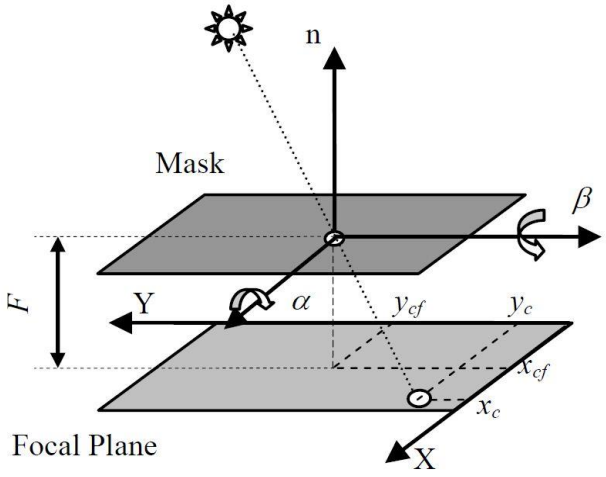

Figure 4. Operating principle of the sensor with one-hole mask. [7]

3 Requirements for the Sun sensors

The E-sail experiment sets the requirements for the ADCS and thus for the Sun sensors. Apart from requirements for the experiment, the Sun sensors must withstand the conditions confronted in LEO and take into account structural restrictions of the satellite in hardware design.

For centrifugal tether deployment the satellite is required to spin-up: reach angular velocity around the satellite z-axis equal to ~360 º/s and align its spin axis with the Earth's polar axis with a pointing error less than 3º. The experiment phase will be performed ~10º from poles where the magnetic field is considered parallel to the spin-plane. The attitude should be estimated with accuracy of 5º. Derived from given restrictions for determination of the attitude, Sun sensors are required to measure the direction of the Sun with accuracy better than 3º per axis.

In order to fit the Sun sensor between the solar cells, the external width of sensors must be less than 14 mm and length less than 25 mm. The electronics board of the Sun sensor must be less than 25 mm wide, 30 mm long and 4.5 mm high.

Since the satellite is required to perform high rate spin control (~360 º/s), Sun sensors as well as magnetometers and gyroscopes are required to have high sampling frequency (order of magnitude 10 Hz).

Each Sun sensor should have the FOV approximately ±45º to be able to provide measurements in any orientation.

Since the power consumption and the mass budget of ESTCube-1 are limited, each sensor should consume power less than 100 mW and weigh less than 10 g.

Optimal ratio between the price and performance requirements of the sensor should be found.

The Sun sensors must withstand temperatures in expected temperature range is from −30 ºC to +40 ºC and operate at solar irradiance level of 1366 W/m^2 (defined as the solar constant) [8, 9].

The sensors must withstand Ultraviolet (UV) radiation in the wavelength range of 100 nm to 400 nm at least for 1 year without malfunctioning. The energy of respective range of solar UV radiation is about 8% of solar constant [9].

4 Use of Sun sensors on CubeSats

This section gives basic overview of implemented Sun sensor concepts by presenting overall technical specifications like dimensions, mass, FOV, power consumption and accuracy.

Two-axis Sun sensors were developed in Technical University of Denmark (DTU) for Danish one-unit CubeSat DTUsat and were also used on SwissCube and COMPASS-1 [10-12]. The devices used on these satellites were a slit type Sun sensors with triangular photodiodes [13]. The photodiodes were fabricated on a silicon-on-insulator type silicon wafer. The lid covering the diode had a well-defined optical slit made with a thin film of gold layer. The sensor's dimensions were 7 mm × 8 mm and had a total weight of 10 g, including printed circuit board (PCB) with dimensions of 7 mm × 39 mm × 50 mm. The accuracy of the given Sun sensor was 3º with a FOV of ±70º. [13]

National Cheng Kung University (NCKU) developed two-axis digital Sun sensors that were used on two-unit CubeSat PACE [14]. A CMOS PSD was used with a pinhole placed above it. The sensor's dimensions were 40 mm × 30 mm × 5 mm and weight was 20 g. The accuracy of the measured angle was estimated to be 0.5º with a FOV of ±60º and power consumption of 200 mW while active. In idle state the sensor consumed 3 mW of power. [15]

Danish AAU CubeSat was one-unit CubeSat that was designed to use one-axis coarse cosine Sun sensors with FOV of ±90º and measurement accuracy of 3.5º [16]. Each side of the satellite had one sensor, while having full coverage of satellites total FOV. The dimensions of the sensors were 10mm × 5mm × 3mm while the mass and power consumption is unspecified. [17]

The Delfi-C3 was a three-unit CubeSat which was launched in 2008 [18]. Although the satellite had no active attitude control, one of the missions was to test autonomous and wireless two-axis Sun sensor, which is based on quadrant PSD, developed by Netherlands Organization for Applied Scientific Research (TNO) [19]. The dimensions of the device were 60 mm × 40 mm × 20 mm and weight was 75 g but no information is provided about the

sensor without its own power source and wireless transmitter unit. The accuracy of the sensor was 0.1º with FOV of ±45º. [20]

The sensor offered by the CubeSatShop consisted of a CMOS PSD detector mounted behind a small pin-hole with a FOV of ±57º. The device produced four analog voltages that are dependant on the angle of incidence of the sunlight in the horizontal and vertical directions. Each sensor was supplied with a calibration algorithm that calculates the Sun vector from these four voltages with accuracy of 0.5º. The dimensions of the device were 33 mm × 11 mm × 6 mm, weight was 5 g and had the power consumption of 50 mW. [21, 22]

5 Design of Sun sensors on ESTCube-1

The ESTCube-1 attitude determination system contains six two-axis Sun sensors. The sensors included in initial trade study were ones developed by DTUsat team, ones developed at NCKU and ones developed by company TNO [15, 20].

Technologies included in initial trade study were charge-coupled device, CMOS, two-axis PSD and one-axis PSD. Digital technologies were not chosen because of higher power consumption. Fulfilling requirements for size and metal or ceramic package, PSDs included in initial trade study were Hamamatsu S3931, S3932, S2044, S5990, S5991, S3979 (out of production) [23-27]. Hamamatsu S3931 was chosen to limit the risk of fitting PSDs in required size of electronics board.

Figure 5 shows the layout of the Sun sensor hardware. Two PSDs are located under a mask with two slits perpendicular to corresponding PSD. Light beam travels through the slit and when reaching the PSD, introduces photocurrent. Depending on the position and intensity of light, two output signals are generated that are converted to voltages and measured by using an Analog-to-Digital Converter (ADC). The position of the light spot on the PSD was calculated by using formula in the datasheet of Hamamatsu S3931 PSD [23]. From the recognition of the light spot on the PSD, the direction of the Sun was calculated.

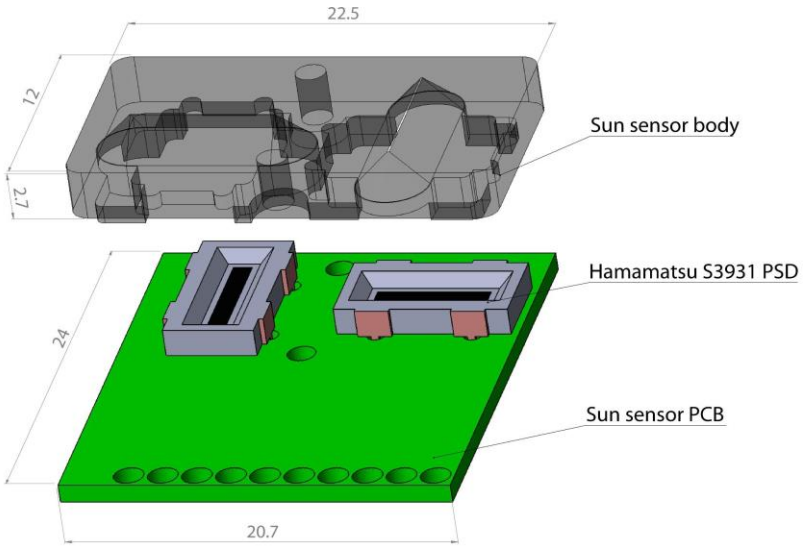

Figure 5. The layout of the Sun sensor hardware.[†]

5.1 Hamamatsu S3931 position sensitive device

Hamamatsu S3931 PSD is a photodiode that consists of a uniform resistive layer formed on one or both surfaces of a high-resistivity semiconductor substrate, having a pair of electrodes formed on the both ends of the resistive layer for extracting the signal for the position of the light spot. The active area, which is a resistive layer, has a PN junction that generates photocurrent by means of the photovoltaic effect. Figure 6 shows the basic structure of S3931 PSD. [23]

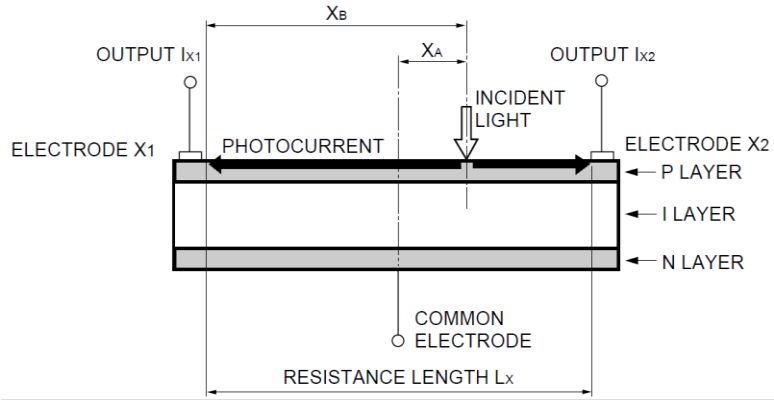

Figure 6. Structure of S3931 PSD. [23]

[†] Figure by Erik Kulu.

When the PSD is illuminated by the light spot, an electric charge proportional to the light intensity is generated at the incident position. This electric charge is driven through the resistive layer and collected by the output electrodes X1 and X2 as photocurrents, while being divided in inverse proportion to the distance between the incident position and each electrode. [23]

When the center point of PSD is set at the origin of position, the relation between the position of incident light and the photocurrents from the output electrodes X1, X2 is

$$P_I = \frac{I_2 - I_1}{I_2 + I_1} \cdot \frac{L}{2} \tag{5.1}$$

where I_1 and I_2 are output currents, L is resistance length of PSD, P_I is calculated position on PSD. [23]

The essential part for all tests, where light illumination is included, is to test the sensor under irradiance level, which is as close as possible to the irradiance value in space at given spectrum. To verify that if the PSD receives approximately same amount of energy in lab conditions as it does in space, the spectral responsivity (photosensitivity) the PSD and spectral irradiance received by the PSD must be known. Photosensitivity of the S3931 PSD is shown in the Figure 7. The cutoff wavelength is determined by the intrinsic material properties of the photodiode, but it is also affected by the spectral transmittance of the light input window material which covers and protects the PSD [41]. For the S3931 PSD, a plastic resin coating is used and wavelengths below 300 nm are absorbed by the coating, causing the decrease of the sensitivity at short-wavelengths [41].

The photocurrent that is produced by the PSD can be found from the equation

$$I_P = \int_0^\infty E_{e\lambda} \cdot R \cdot d\lambda \tag{5.2}$$

where $E_{e\lambda}$ is the spectral irradiance of the sensor, R is spectral responsivity of PSD, λ is wavelength of incident light.

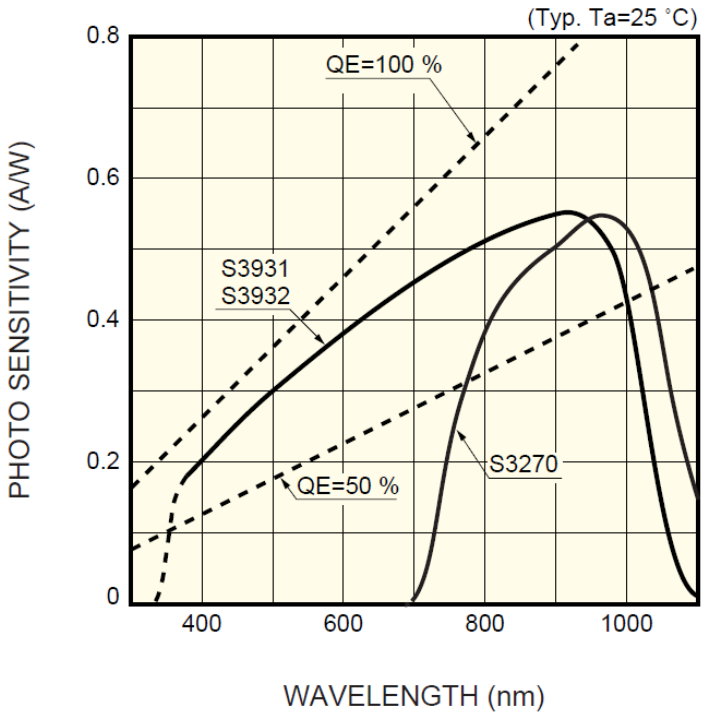

Figure 7. Photosensitivity of S3931 PSD. [23]

5.2 Mask

The mask of the sensor, which is depicted in Figure 8, is designed to fit on the PSDs as tightly as possible, to minimize unwanted effects arising from mispositioning the slit over the PSD, which is discussed further in the chapter 6.1.3. The mask is black anodized, in order to reduce reflections from inner surfaces. The optimal width of the slit is approximately 0.1 mm, which was calculated by taking into account the loss of position measurement resolution due to diffraction effects.

Optimal width of slit was calculated by considering the following:

- The FOV is 90°,
- PSD is 6 mm long,
- Mean wavelength of the incident light is 800 nm,
- Width of the slit must equal to the distance between first minimum of the diffraction on the PSD at the FOV/2 incident angle,

- Angle of the first minimum of diffraction is

$$\varphi = a\sin\left(\frac{\lambda}{b\cdot\cos\left(\frac{\mathrm{FOV}}{2}\right)}\right) \tag{5.3}$$

where λ is wavelength of incident light, b is width of the slit, FOV is field of vision (90°).

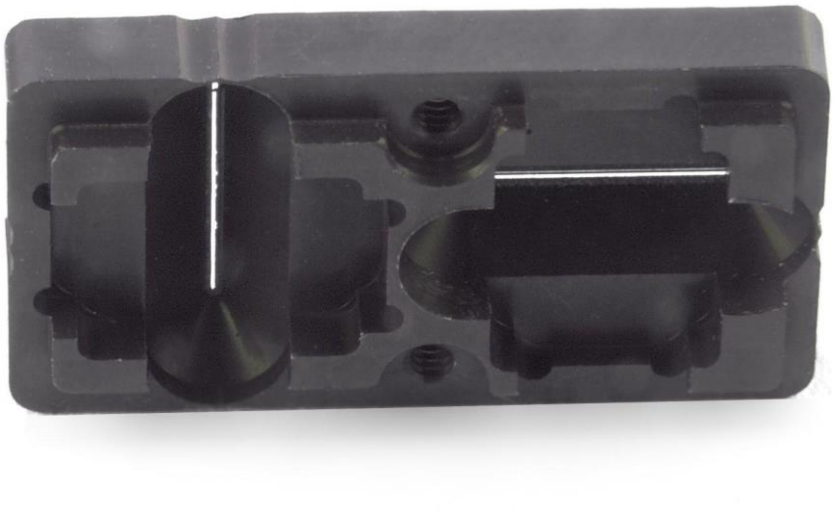

Figure 8. Final design of the mask.[†]

5.3 Electrical design

Figure 9 depicts the electrical layout of the Sun sensor. Only one PSD is presented on the Figure 9 since the circuits are identical for each PSD. Each output of the PSD is connected to a Current-to-Voltage Conversion (CVC) circuit that outputs the difference between supply voltage and converted input signal. This differential signal is measured with 12 bit MAX1230 ADC [28]. Capacitors are used to filter out the noise. The CVC circuit is optimized to produce highest possible output voltage in LEO while avoiding saturation of output signal with a safety margin of 40%. The maximum sampling rate of MAX 1230 ADC is 300 000 samples per second (sps) [28]. Two ADCs are used, as 3 Sun sensors are connected to one ADC. Each Sun sensor has 4 analog outputs and therefore the total amount of output signals to measure per one

[†] Photo by Henri Kuuste.

ADC is 12 and 20 samples are needed for averaging per each channel. Therefore the maximum sampling rate is

$$\frac{300\text{ksps}}{12 \cdot 20} = 1.25\text{ksps} \tag{5.4}$$

Thus the requirement of having sampling rate in the order of magnitude of 10 Hz is satisfied.

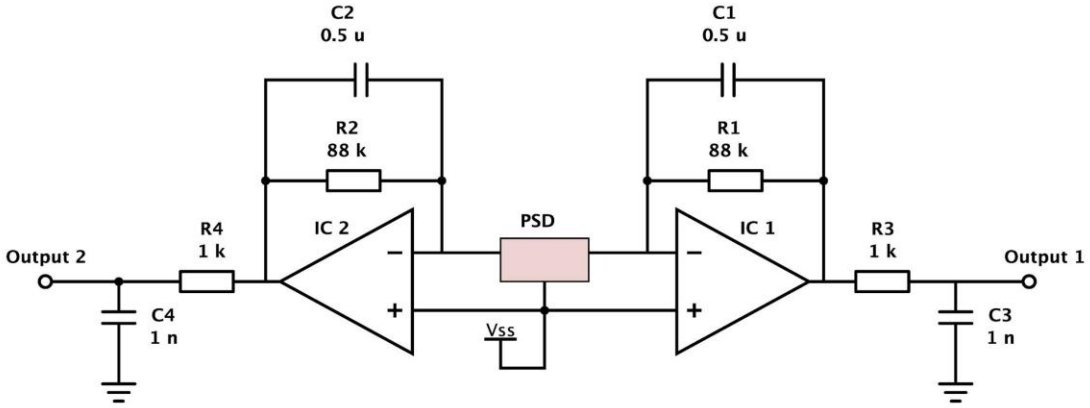

Figure 9. Electrical layout of the Sun sensor.

Since the CVC circuit outputs the difference between supply voltage and converted input signal, the position calculation equation (5.1) must be modified to

$$P_U = \frac{(U_S - U_2) - (U_S - U_1)}{(U_S - U_2) + (U_S - U_1)} \cdot \frac{L}{2} \tag{5.5}$$

where U_S is supply voltage, U_1 is output voltage 1, U_2 is output voltage 2.

5.4 Mass and power budget

Table 1 presents the mass budget and Table 2 presents the power budget of the Sun sensor. The mass of the components of the Sun sensor were measured in laboratory, whereas the power consumption of the sensor was estimated from direct measurements and the data provided from the datasheets of the components.

Table 1. Mass budget of the Sun sensor.

Component	Qty	Mass (g)
PSD	2	2 × 0.2
Mask	1	1.6
PCB	1	1.9
Set of electrical components per sensor	1	0.7
Sun sensor	**1**	**4.6**

The mass of the Sun sensor is 4.6 g which fulfills the requirements.

Table 2. Power budget of the Sun sensor.

Component / name	Qty	Average power (mW)	Max power (mW)
ADC / MAX 1230 + supporting components[†]	1/3[††]	13.3[‡]	20
Op-amp / OPA 4344 [29]	1	3[◊]	5[◊]
Voltage regulator / LP2985AIM5-4.5 [30]	1	<1[◊]	6[◊]
PSD / S3931	2	0	0
Sun sensor	**1**	**~16[‡]**	**~30**

The average power consumption is ~16 mW with peak value of 30 mW, which satisfies the requirements.

[†] Reference voltage, Reference voltage charge pump, Level converter (5V serial peripheral interface to 3.3 V serial peripheral interface).
[††] Three Sun sensors per one ADC.
[‡] Measured in laboratory.
[◊] Given in datasheet

6 Testing and characterization of Sun sensors

The main outcome of this work is to have LEO qualified device and therefore a variety of tests that indicate the reliability in required conditions were carried out. The main influential factors are the temperature, radiation intensity, pressure and sensors geometrical, optical and electrical properties that deviate the performance of the sensor from idealistic model. Thus besides the above mentioned main influential factors, the sensors angular response characteristics and output noise was needed to be considered to estimate the behavior and output uncertainty of the device. Tests, results, evaluation of uncertainty and calibration process of Sun sensors are described further in this section.

6.1 Testing of Sun sensors angular response

The process, where Angular Response (AR) of the Sun sensor is tested (further referred as AR test), is a process where the sensor is rotated in front of a light source and the output that depends on the angle of incidence of light is measured. AR tests measures angular response characteristics of the sensor in different environmental conditions of interest.

6.1.1 Test setup

The test setup, which is listed in the Table 3, is presented on Figure 10. A sun sensor (1) was fixed on a rotating bench (2) and illuminated by a light source (3). For aligning, a laser (4) was used. Sensors outputs were converted by an ADC on the electronics board (5) and digitized data was sent to a computer (6) for processing. The computer also controlled the rotating bench through a controller (7).

The test was carried out by turning the rotation bench and measuring the output signals of the sensor. The sensor was altogether rotated for ±60° in steps of 0.5° and 20 measurements were taken per each stop. The rotation angle was measured between PSD's surface normal and optical axis (angle of incidence).

The testing process was following:

1. The sensor was adjusted to be on the optical axis for all rotation angles,
2. The sensor was adjusted perpendicularly in front of the light source (angle of incidence equal to 0°),
3. The sensor was rotated "+" or "-" 60°,
4. 20 output voltage measurements were taken,
5. The results were added to a measurement log file,
6. The sensor was rotated for 0.5°,
7. Steps 4 to 6 were repeated until the sensor was rotated for 120°.

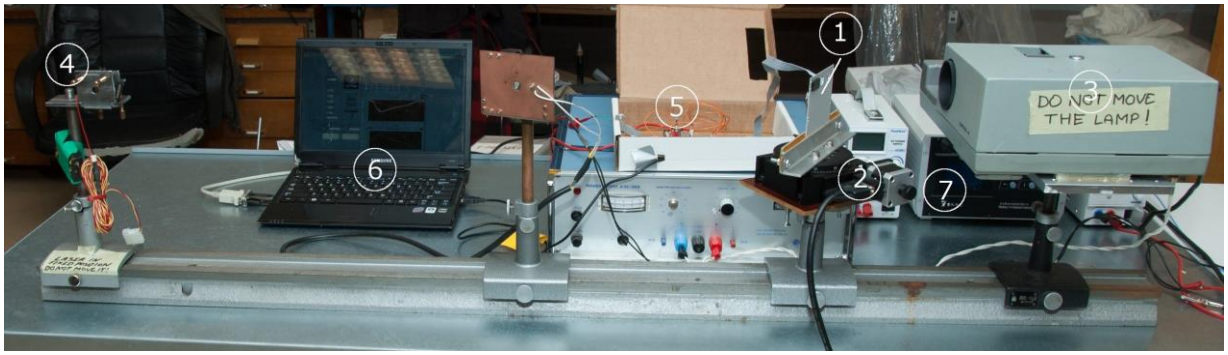

Figure 10. Sun sensor angle test setup: Sun sensor (1), rotating bench (2), light source (3), laser (4), electronics board (5), computer (6), rotating bench controller (7).[†]

Table 3. List of angular response test equipment.

Device nr	Name of device	Descriptions
2	Rotating bench MOR-100 [31]	Resolution – 1/200°
3	Light source	Halogen lamp, Power 180 W
5	Electronics board	ESTCube-1 Flight model ADCS board
7	Controller of rotating bench MOC-3 [32]	---

The Halogen lamp had parabolic reflectors, producing approximately planar profile of light. Laser was used to align the lamp on optical axis and therefore the sensor received light with its profile being efficiently as planar.

[†] Photo by Henri Kuuste.

6.1.2 Software

The controller of rotation bench received commands from the computer through RS232 port. LabVIEW 2011 software developing environment was used as main commanding platform of the AR test [33]. Figure 11 shows the user interface of the program.

The main functions of the AR test software were to

- Control the rotation bench,
- Read and analyze the measurements of Sun sensors,
- Store recorded data for further analysis.

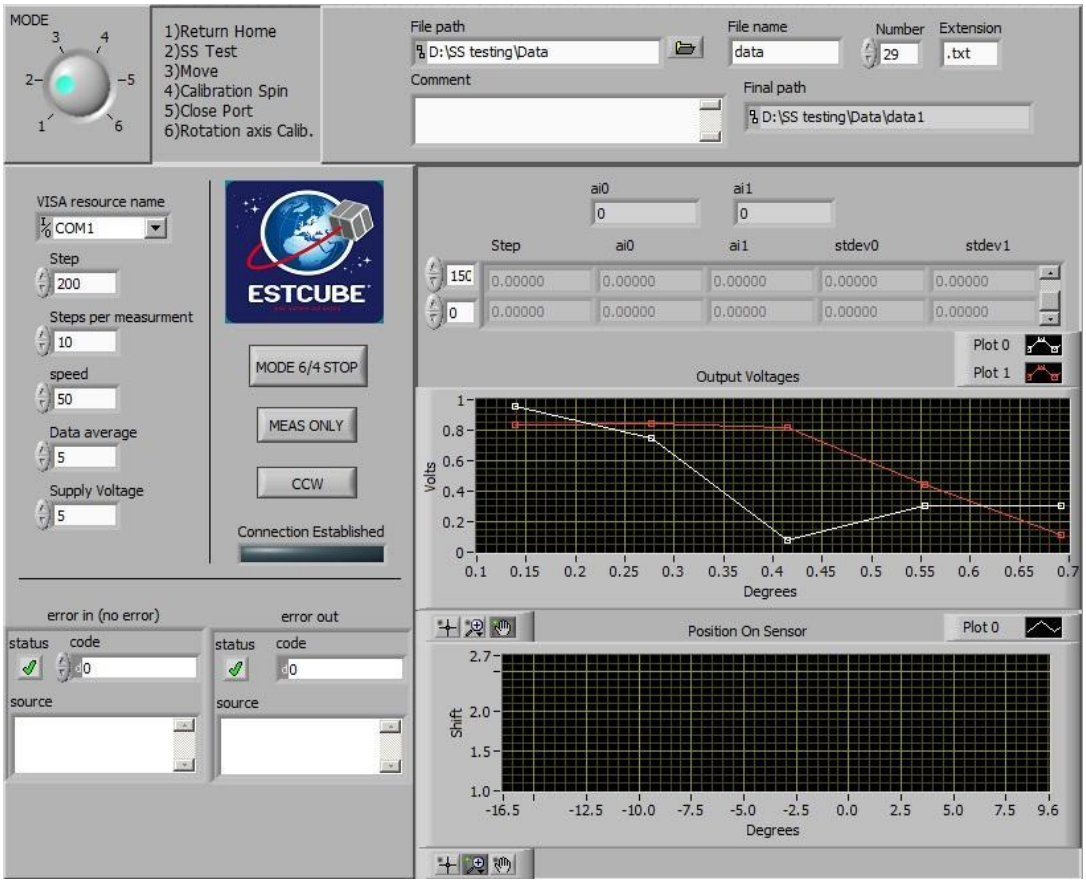

Figure 11. AR test software interface.

6.1.3 Model of angular response test

The objective of modeling is to predict the outcome of the AR test. The model of the AR test consists of two separate parts where one describes the behavior of output voltages and the other model describes the relation between angle of incidence of light (further referring as angle of incidence) and measured position of light on the PSD (further referring as position on the PSD).

Model for position measurements of angular response test

In modeling the dependency between the angle of incidence and lights position on the PSD, the rotation bench is assumed to rotate the sensor with constant change of angle of incidence. Therefore the angle of incidence is changed linearly. Figure 12 shows the basic geometrical relations that the model is based on. If the height of the slit from the PSD is known, the angle of incidence dependent position on the PSD is

$$pos(\alpha) = h \cdot \tan(\alpha) + \Delta p\,, \tag{6.1}$$

where $pos(\alpha)$ is the position of the light spot on the PSD, α is the angle of incidence of light, h is the distance between the slit and the PSD, Δp is the drift of the position.

Drift of the position Δp takes into account the fact that the mask may not be positioned symmetrically over the PSD which means that if the sensor is illuminated at 0° angle, the light strip does not illuminate the center of PSDs sensitive area (resistance length).

If the angle of incidence reaches the limit of FOV, light starts to be reflected from the mask as shown on Figure 12 as light beam with incident angle β. The position of reflected light on the PSD is

$$pos(\alpha)_R = \left[h\sqrt{2} - w \cdot \frac{\cos(\alpha)}{2\sin(\gamma(\alpha))} \right] \cdot \frac{\sin(\gamma(\alpha))}{\sin(\varphi(\alpha))} \tag{6.2}$$

where $pos(\alpha)_R$ is the position of the reflected light on the PSD, α and β are angles of incidence, W, γ, φ are geometrical relations of the Sun sensor (shown in Figure 12).

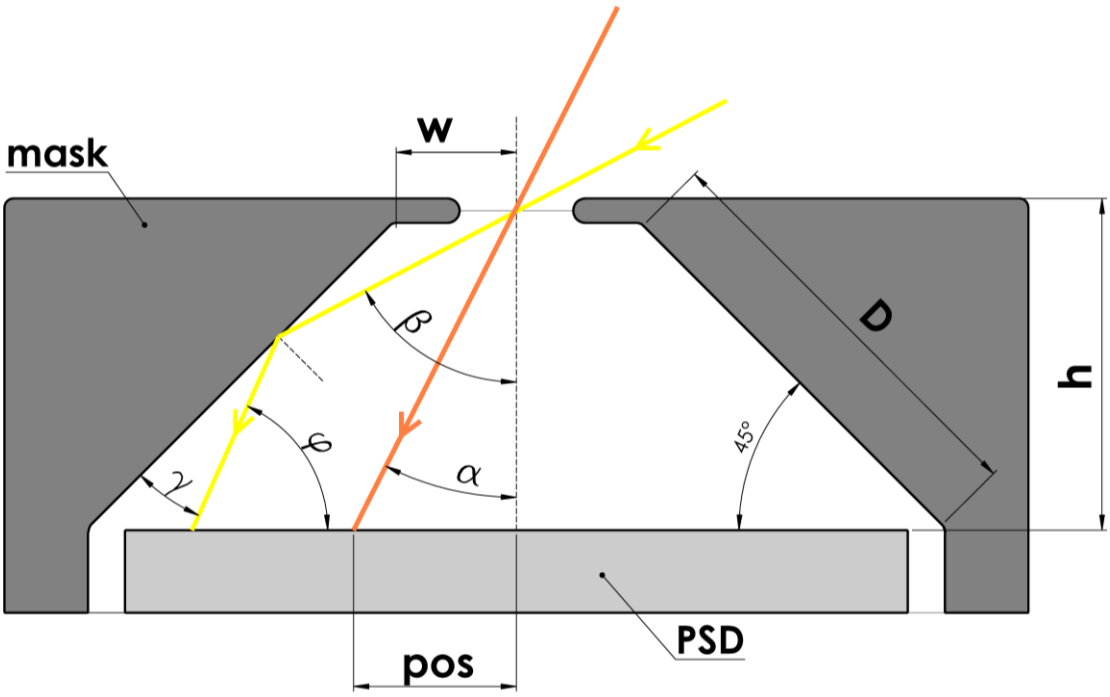

Figure 12. Geometrical relations that are taken into account in modeling of position of reflected incident light on the PSD.

When the limit of the FOV is reached, there is a small transition region, where amount of not reflected light (light beam with incident angle α in Figure 12), decreases while amount of reflected light increases. This results a small transition region between direct and reflected light.

The results of the model for position measurements of angular response test, where geometrical dimensions of the mask were used in modeling process, are presented in Figure 13.

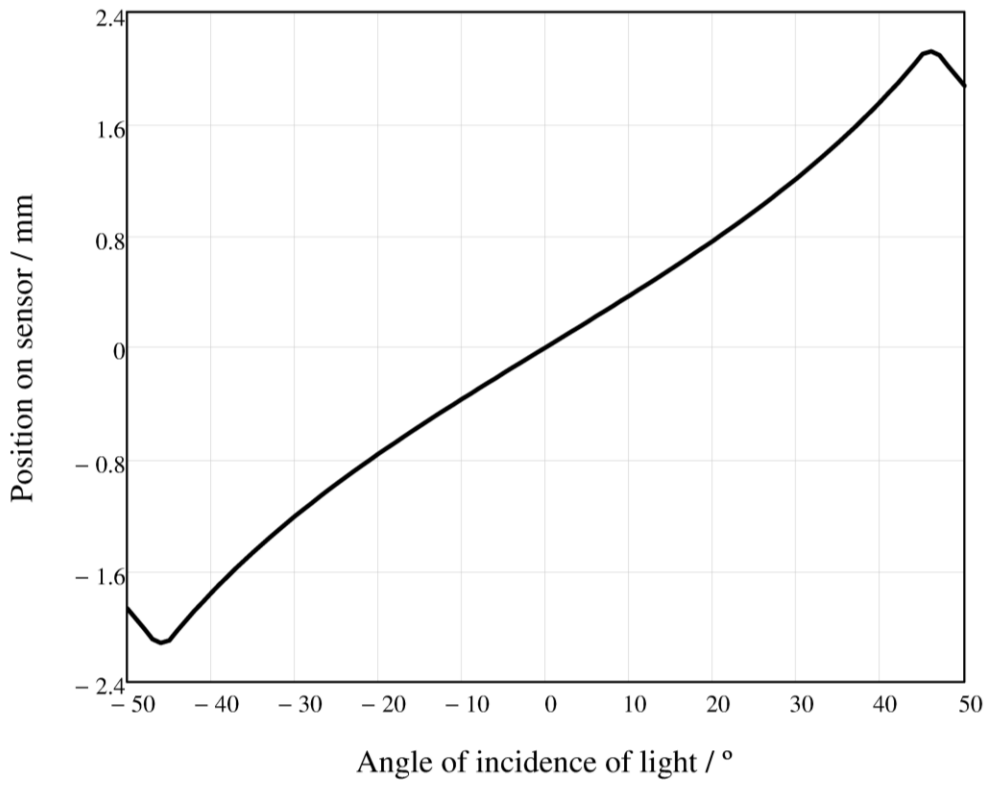

Figure 13. Result of modeling the dependency between the angle of incidence of light and position on the PSD.

Model for the output signals of the Sun sensor

The model for the output signals of the Sun sensor is based on the geometrical properties of the sensor. The model takes into account the fact that the net photocurrent (sum of two output currents) depends on intensity of the incident light (further referred as the intensity) and stays at constant value if the intensity does not change. Also the net photocurrent is proportional to cosine of angle of incidence [5].

The basic form of the model for the output signals of the Sun sensor is

$$O_1(\alpha) = U_S - \left[U_P \cdot INT(\alpha) \cdot \frac{POS(\alpha + \Delta\alpha)}{L} \right], \tag{6.3}$$

$$O_2(\alpha) = U_S - \left[U_P \cdot INT(\alpha) \cdot \left[1 - \frac{POS(\alpha + \Delta\alpha)}{L} \right] \right] \tag{6.4}$$

where O_1 is output 1, O_2 is output 2, α is the angle of incidence, U_S is supply voltage, U_P is sum of output voltages in 0° angle of incidence, $INT(\alpha)$ is a coefficient that estimates how much light passes through the mask, $POS(\alpha)$ is lights position on the PSD, L is resistance length of PSD, $\Delta\alpha$ characterizes the drift of the position.

The position on the PSD, $POS(\alpha)$, is essentially same as the model for position measurements of AR test. The only difference is that for $POS(\alpha)$ the point of origin of the coordinates is the end point of the resistance length L, not the center point.

The coefficient for relative intensity of light, $INT(\alpha)$, gives an estimate about how much light passes through the mask by taking into account the net photocurrent's proportionality to cosine of angle of incidence and the thickness of the mask's slit. Net photocurrent's proportionality to cosine of angle of incidence can be depicted as variation of effective width of slit. The idea of effective width of slit is presented in Figure 14. When sensor is illuminated with the angle of incidence being equal to 0º, the amount of light that passes through the slit is maximal. The amount of passing light starts to decrease when the angle of incidence differs from 0º.

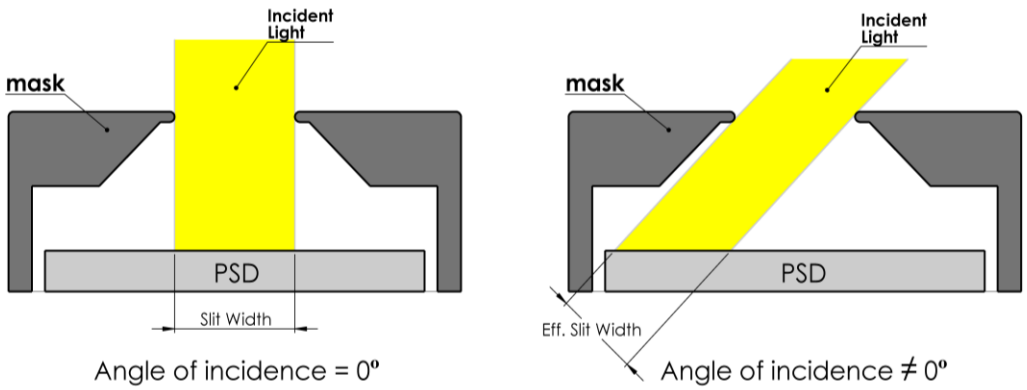

Figure 14. The amount of light that passes through the slit is maximum when the angle of incidence is 0º. When illuminated at non 0º angle, the effective width of slit and therefore the amount of passing light decreases.

Since the edges of the slit have a finite thickness, which is approximately half of the slit's width, some of light is also blocked by the edges of the slit. In the model, the edges are assumed to be perfectly round with radius half of mask's thickness. The idea of the edges of the slit blocking incident light is shown in Figure 15 where α is the angle of incidence.

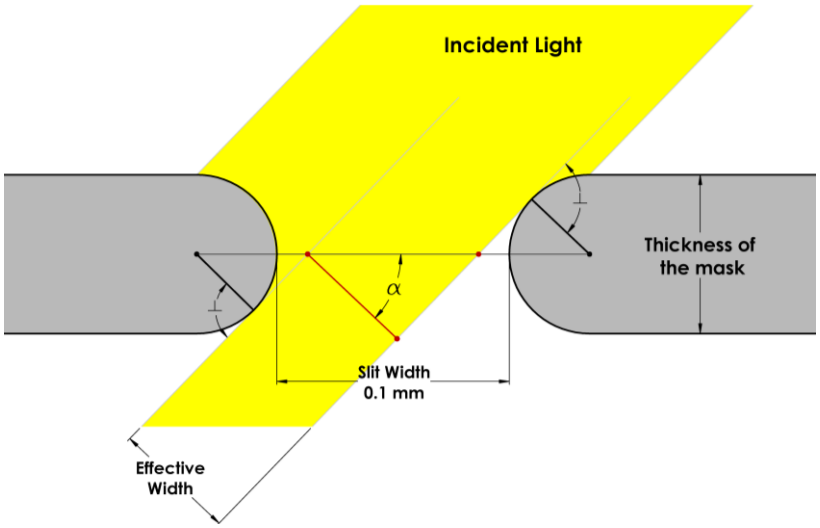

Figure 15. Some amount of light is blocked by the edges of the slit, which are assumed to be perfectly round in the model.

As a result of considering the effective width of slit and thickness of the mask to influence the amount of light that passes through the slit, the relation between maximum (0° angle of incidence) and minimum (±45° angle of incidence) amount of light in the region of FOV is

$$INT(\pm 45°)\times 100\% = \left[\cos(\pm 45°) - \frac{1}{2}\left[1-\cos(\pm 45°)\right]\right]\times 100\% = 56.1\%. \qquad (6.5)$$

Due to varying intensity, output signals don't change linearly with a linear change of position of incident light on the PSD. Furthermore, according to AR test position measurement model the relation between change of angle of incidence and the position on the PSD is nonlinear. This causes additional nonlinearities in the relation between the angle of incidence and output signals of the PSD.

Light starts to be blocked by the mask when the angle of incidence exceeds ±45°. Yet some part of the light reflects back to the PSD and the portion of reflected light is growing as direct light is being increasingly blocked due to the limit of FOV.

There is also a possibility, that the mask is positioned asymmetrically over the PSD. In output signal model, this asymmetrical positioning corresponds to a phase shift $\Delta\alpha$ between the change of effective width of slit and lights position on the PSD that ultimately results an inequality between the minimum values of the two measured output signals.

The results of the model for the output signals of the Sun sensor are shown in Figure 16.

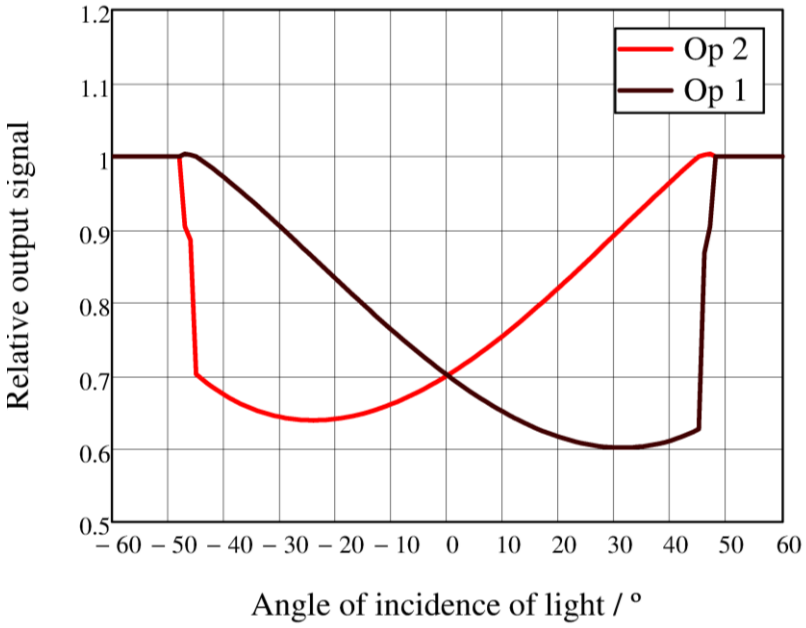

Figure 16. Results of the model for Sun sensor's output signals.

6.1.4 Test results and comparison with the model

Figure 17 shows comparison between the results of AR test position measurements and the respective model. It can be seen that the measured results are characteristically similar to the model, as the measurements are slightly nonlinear and reflections appear outside the region of FOV but there is no direct coincidence with measured data and the model, due to unknown influential factors. The influential factors to measurement nonlinearities might be the level of irradiance and the protective resin coating of the PSD that refracts light. Also Figure 17 shows that the center of PSD's sensitive area may not coincide with the apparent position that was measured in perpendicular state between PSD's surface and optical axis. This is probably caused by asymmetrical positioning of the mask over the PSD which was discussed in output chapter 6.1.3.

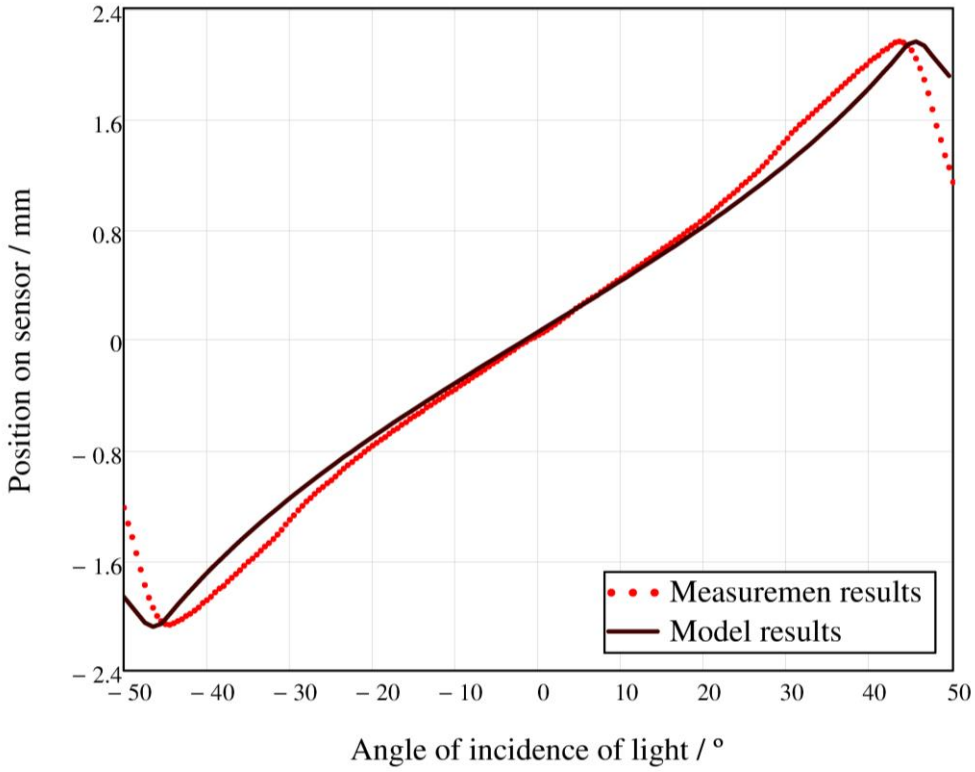

Figure 17. Measured dependency between the position of incident light and rotation angle compared to the results of position measurement model.

Figure 18 shows the output voltages of the same AR test that is presented in Figure 17. It can be seen that output signals are nonlinear and the minimum value of each output is different for the given sensor, as predicted in the model. In the region of -25° to 25° the slope of the change of voltage decreases, which can be caused by saturation of the photocurrent, since the amount of light passing the slit is depending on incident angle. Saturation of photocurrent is equivalent to effectively constant intensity of incident light and therefore outputs are changing linearly.

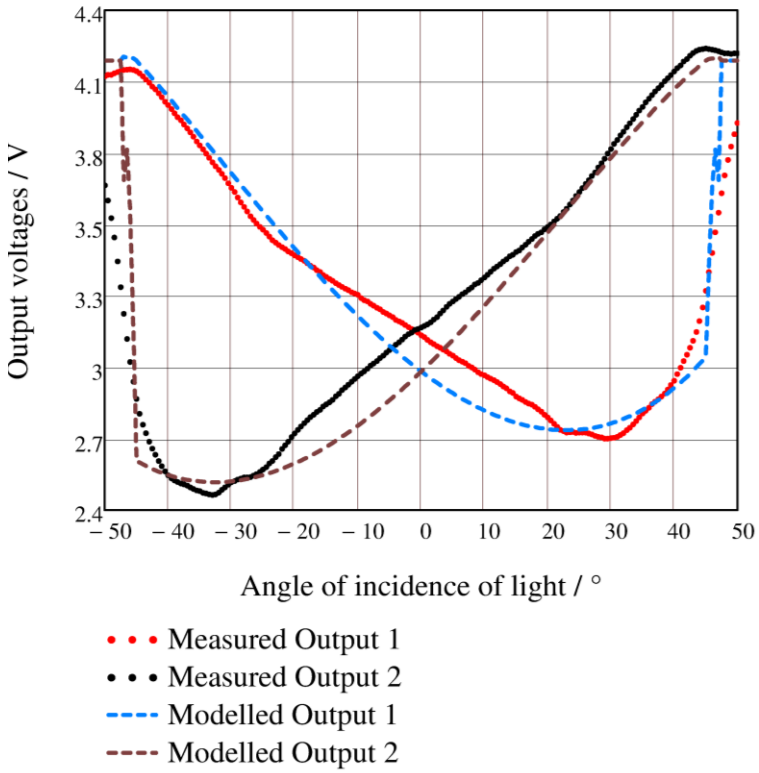

Figure 18. Measured dependency of Sun sensors output signals on angle of incidence compared to the model.

6.1.5 Uncertainty evaluation

The main contributors to the uncertainty of AR tests are

- Repeatability of the Sun sensor's measurement results,
- Precision of the AR test equipment,
- Rotation resolution of the rotation bench.

Position to angle coefficient

AR tests give information about light's position on the PSD. Since the objective of the Sun sensor is to determine the direction of a light source, the uncertainties must also be presented in degrees. AR tests connect the measured position with incident angle of light and therefore AR tests are used to find the sensitivity coefficient between measured position on sensor and incident angle of light, further referring as Position to Angle (PTA) coefficient.

As presented in the Figure 17, the dependency between the measured position and angle of incidence is nonlinear which means that the slope or the PTA coefficient of given dependency is depending on angle of incidence, but it can be approximated by finding linear fit to the data of the AR test in the acceptable uncertainty limits.

Figure 19 shows a linear function fitted to the data of AR test measurements. The slope of regressed function is

$$\eta = 21.61 \frac{^\circ}{\text{mm}}. \tag{6.6}$$

Standard deviation of the slope (6.6)

$$s_\eta = 0.09 \frac{^\circ}{\text{mm}} \tag{6.7}$$

is small enough to give no significant contribution to the overall uncertainty budget in Table 5.

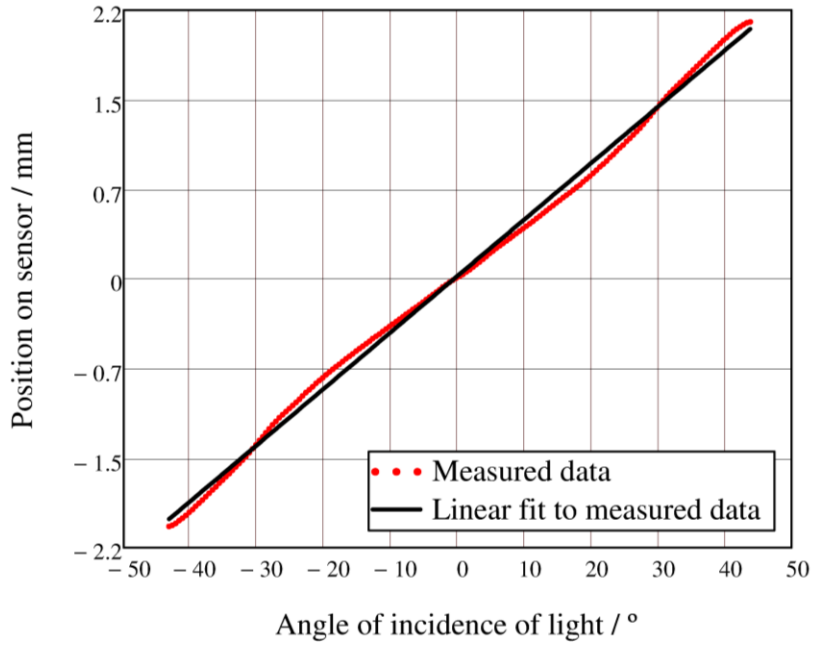

Figure 19. A linear function fitted to the data of AR test measurements.

Uncertainty contribution from repeatability of the Sun sensor's measurement results

Repeatability of the Sun sensor's measurements characterizes all the factors that influence the measurements of the sensor by appearing as noise in the output signal. Figure 20 shows standard deviation of the measurements of position depending on angle of incidence. There is no significant change of standard deviation in the region of FOV but outside this region the deviation starts to increase.

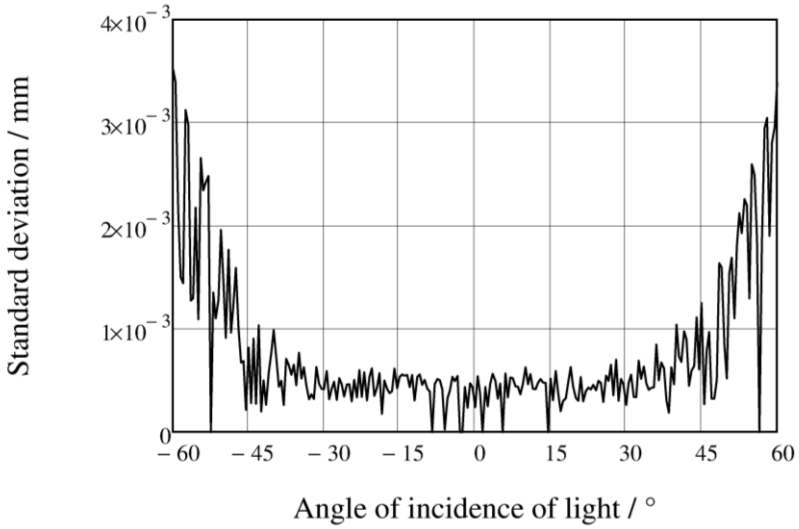

Figure 20. Standard deviation of position measurements depending on rotation angle.

The highest value of standard deviation of position in the region of FOV, which was calculated from 20 measurements, is used to evaluate the uncertainty component of the measurement repeatability, which is

$$s_E = 1\,\mu\text{m} \tag{6.8}$$

and type-A uncertainty component of repeatability is

$$u_{AE\,p} = \frac{s_E}{\sqrt{20}} = 2.24 \cdot 10^{-4}\ \text{mm}\,. \tag{6.9}$$

Converted into degrees:

$$u_{AE} = u_{AE\,p} \cdot PTA = 4.83° \cdot 10^{-3}. \tag{6.10}$$

Uncertainty contribution from digital resolution of the ADC

Output voltages of the Sun sensor are measured with 12-bit ADC with 5V reference voltage. This means that the least significant bit (LSB) in terms of voltage is

$$LSB_U = \frac{5\,V}{2^{12}}, \tag{6.11}$$

but in terms of integers, the LSB is equal to 1.

Accuracy of output measurements is limited with the LSB and to evaluate, how it contributes to the uncertainty of measured position, the partial derivatives of position calculation equation (5.4) with respect to both output voltages must be calculated:

$$\frac{\partial P_U}{\partial U_1} = L\frac{\left(U_2 - U_S\right)}{\left(2U_S - U_1 - U_2\right)^2}, \tag{6.12}$$

$$\frac{\partial P_U}{\partial U_2} = L\frac{\left(U_S - U_1\right)}{\left(2U_S - U_1 - U_2\right)^2} \tag{6.13}$$

where U_S is the supply voltage for the Sun sensor, U_1 and U_2 are output voltages of the sensor.

Uncertainty contribution from the LSB is

$$u_{LSB}(U_1,U_2) = L\frac{\mathrm{LSB}}{\sqrt{12}}\sqrt{\left(\frac{\partial P_U}{\partial U_1}\right)^2+\left(\frac{\partial P_U}{\partial U_2}\right)^2} \tag{6.14}$$

where L is resistance length of the PSD and LSB is least significant bit.

In Figure 21, where presented quantities originate from the same AR test as in Figure 20, shows that in the region of FOV, the uncertainty is practically at a constant value. Near the limits of FOV and further, uncertainty starts to increase because both output signals of the sensor are low and are comparable with the value of the LSB. There are clear similarities between standard deviation of position and type B uncertainty (Equation 6.14), which was calculated by taking only the influence of the LSB into account. Therefore it can be assumed, that the repeatability of the Sun sensor measurement results is mostly influenced by digital resolution of the ADC.

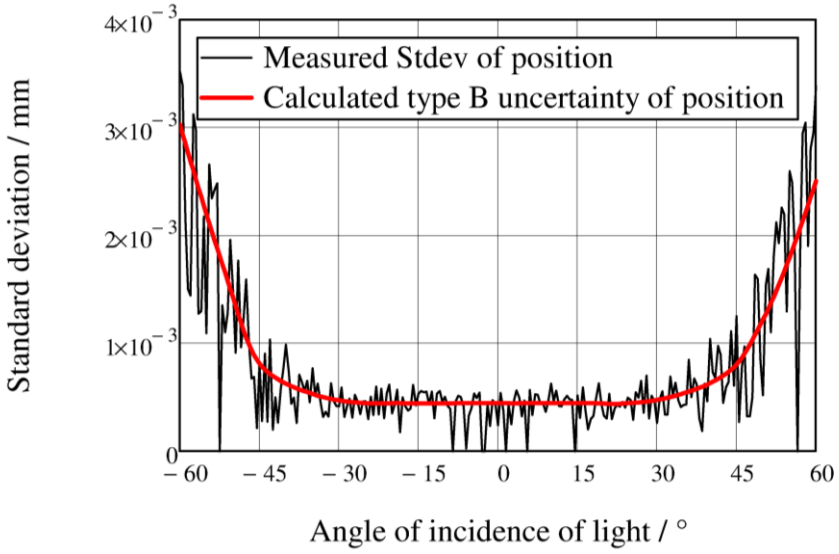

Figure 21. Standard deviation and type B uncertainty of measured position depending on incident angle of light.

The highest value of type B uncertainty component of measured position, caused by digital resolution of the ADC in the region of FOV, is

$$u_{BE\,p} = 7.4\cdot 10^{-4}\ \mathrm{mm}\,. \tag{6.15}$$

Converted into degrees:

$$u_{BE} = u_{BE\,p} \cdot PTA = 16° \cdot 10^{-3}. \quad (6.16)$$

Precision of angular response test equipment

Measured results are expected to vary within the limits of precision of the AR test equipment. For AR test precision estimation, the test setup was disassembled and put back together after each AR test for 6 times.

The testing and analysis was following:

1. The AR test equipment was disassembled,
2. The AR test equipment was reassembled,
3. The equipment was adjusted,
4. AR test was carried out,
5. Steps 1 to 4 were repeated for 6 times
6. The mean values of all 6 test results were compared,
7. Standard deviation of 6 measured AR test position values were calculated per all rotation angles.

Figure 22 shows the standard deviations between measured position values of 6 AR tests.

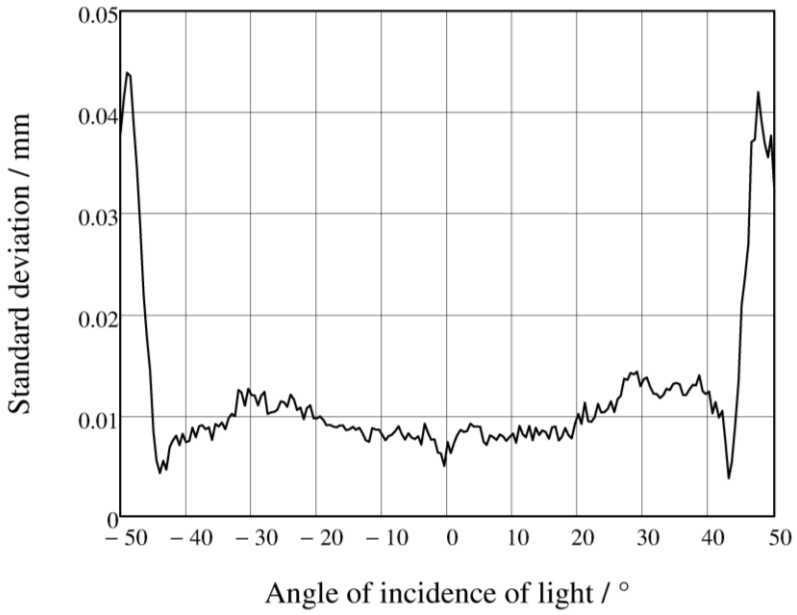

Figure 22. Standard deviation of apparent position of 6 AR tests depending on angle of incidence.

The highest value of standard deviation of repeatability in the region of FOV is used to evaluate the uncertainty component of AR test precision. Highest value of standard deviation in region of FOV is

$$s_{\mathrm{Re}} = 9.2 \cdot 10^{-3} \text{ mm}. \tag{6.17}$$

Uncertainty component of precision is

$$u_{\mathrm{Re}\,p} = \frac{s_{\mathrm{Re}}}{\sqrt{6}} = 3.75 \cdot 10^{-3} \text{ mm}. \tag{6.18}$$

Converted into degrees:

$$u_{\mathrm{Re}} = u_{\mathrm{Re}\,p} \cdot PTA = 0.081°. \tag{6.19}$$

Uncertainty component from rotation bench's resolution

The resolution of the rotation bench defines the smallest angle of rotation that can be made with the bench, which is

$$\Delta_R = \frac{1}{200}°. \tag{6.20}$$

Uncertainty contribution from rotation bench's resolution is type B uncertainty and therefore it is calculated as

$$u_R = \frac{\Delta_R}{\sqrt{12}} = 1.44° \cdot 10^{-3}. \quad (6.21)$$

6.2 Thermal influence test

The thermal influence tests provide information about the effect of ambient temperature on performance of the Sun sensors. The expected temperature range in LEO is from −30 ºC to +40 ºC [8].

6.2.1 Test setup

Figure 23 shows the setup of the thermal influence test. A Sun sensor (1) in a thermal chamber (2) is illuminated through side port (3) of the thermal chamber with a light source (4). Three calibrated temperature sensors (5) are used. All readings are gathered by a Data Acquisition device (DAQ) (6) and processed by a computer (7). The angle of incidence is constant throughout the test. The components of the setup are listed in table 4.

The testing process was following:

1. The Sun sensor with 3 temperature sensors was placed into the thermal chamber,
2. The chamber was closed and the light source was turned on,
3. The initial temperature of the test was set to be 80 °C,
4. The outputs of the temperature sensors and the Sun sensor were measured,
5. The temperature was decreased to −15 °C and during cooling process, the outputs of the sensors were measured,
6. The test was repeated for different angles of incidence.

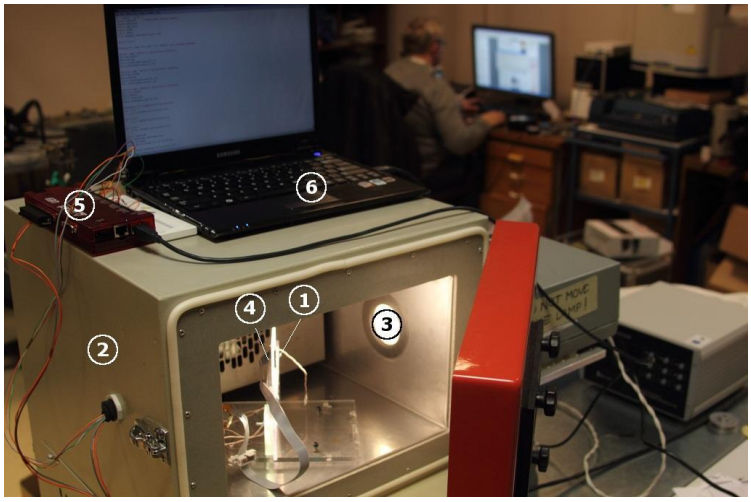

Figure 23. Sun sensor temperature test setup: Sun sensor (1), thermal chamber (2), side port (3), light source (4), temperature sensors (5), DAQ (6), computer (7).

Table 4. List of temperature test equipment.

Device nr	Device	Descriptions
2	Thermal chamber	Heraeus Votch VMT 04/16 [35]
3	Light source	Halogen lamp, Power 180 W
4	Temperature sensors	KTY82-1 [43]
5	DAQ	Labjack UE9 [34]

6.2.2 Results and analysis

Three temperature tests were performed with angles of incidence approximately −30°, 0° and +30°. The achievable lower limit of temperature was about −10 °C. In case if the higher expected thermal limit should be exceeded in space, the upper limit of testing was chosen to be 80 °C. Figure 24 shows the drift of calculated position due to change of temperature for all three incidence angles. These results indicate that apparent position of light shifts with temperature.

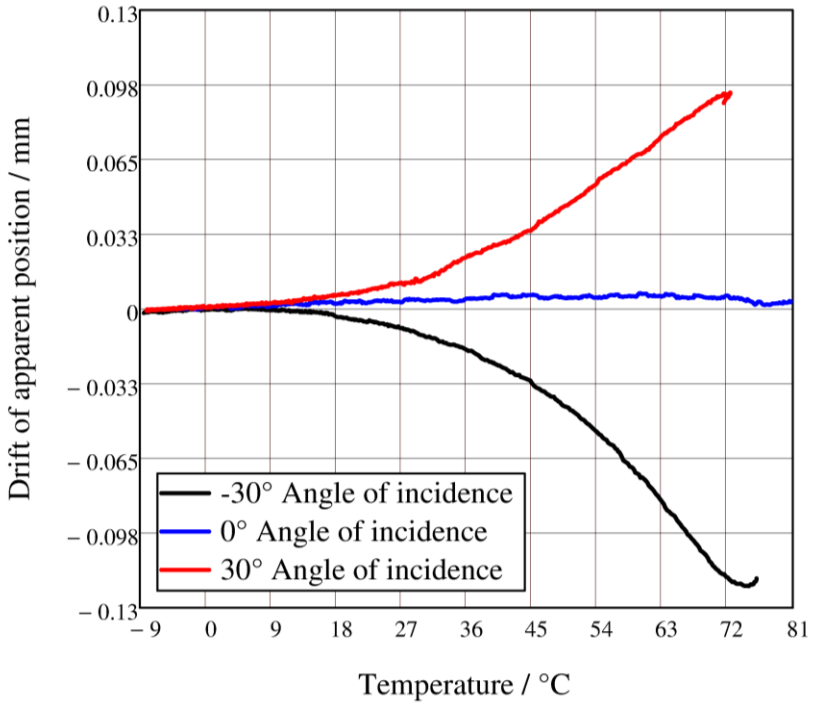

Figure 24. Drift of calculated apparent position due to change of temperature.

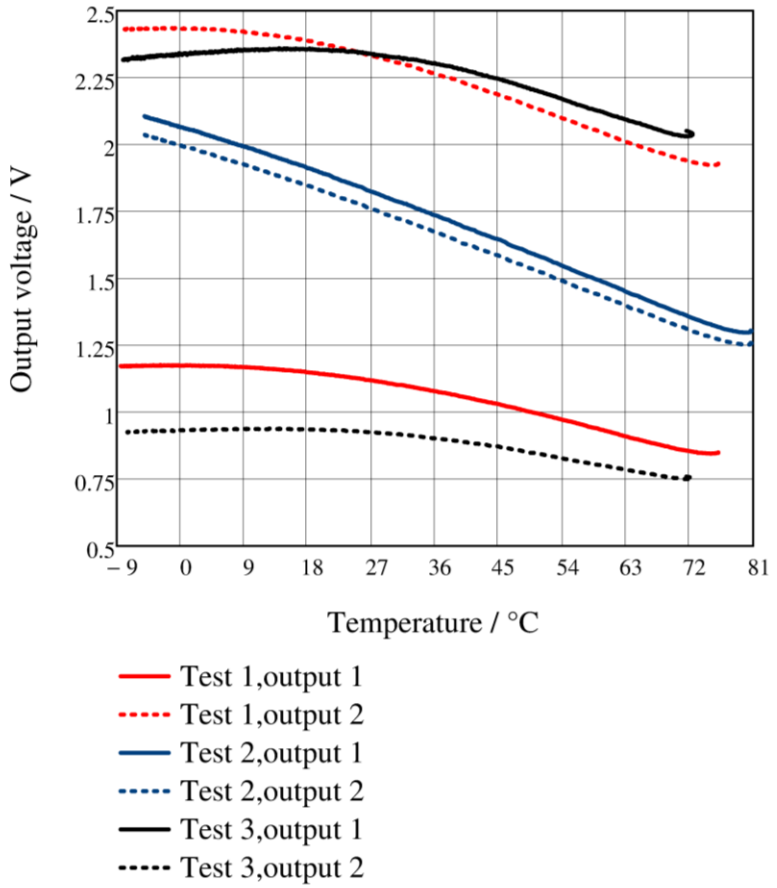

Figure 25. Shift of output voltages due to change of temperature.

6.2.3 Uncertainty evaluation

Since the Sun sensors don't have a temperature sensor onboard, the difference between maximum and minimum value of temperature contributes as type B source of thermal uncertainty. Difference between maximum and minimum value of temperature is

$$\Delta_T = 84\,°\mathrm{C}\,. \tag{6.22}$$

The difference between maximum and minimum value of apparent position in respective range of temperature is

$$\Delta_{PT} = 0.12\ \mathrm{mm}\,. \tag{6.23}$$

Uncertainty of measured position due to temperature is

$$u_{PT} = \frac{\Delta_{PT}}{\sqrt{12}} = 0.035\,\text{mm}\,. \tag{6.24}$$

Converted into angular degrees:

$$u_T = u_{PT} \cdot PTA = 0.755°\,. \tag{6.25}$$

In further perspective, for minimizing the thermal influence, a complex theoretical model of Sun sensor should be constructed in addition to including temperature sensors on Sun sensor PCB.

6.3 Testing of angular response to varied irradiance

The reason for the varied irradiance test is to indicate the possibility of saturation of the PSD or any other phenomena. The AR test setup is used to measure the AR of the Sun sensor to given irradiance level produced by lamp with known spectrum at fixed distances. The test results are used for optimizing electronic design by choosing components to withstand the expected irradiance level in space, which is 1366 W/m^2 [9].

6.3.1 Testing procedure

Testing procedure consists of 4 separate angle tests, where irradiance is raised from 1000(50) W/m^2 to 1800(50) W/m^2 and kept constant throughout a single test.

The testing process is following:

1. The Sun sensor was placed at a position, where lamp's spectrum was known,
2. The AR test process was carried out,
3. The test was repeated with a different value of light source's irradiance.

6.3.2 Results and analysis

The measurement data from 4 AR tests were compared and the difference between maximum and minimum values of measured position was calculated per each angle of incidence, which

are presented in Figure 26. In AR tests the spectrum of the light source is known at fixed distances, but to take into account the fact that the actual solar irradiance confronted in LEO may differ from the one that is produced by the lamp, the highest value of the difference between the measurements is taken into account as an uncertainty component from solar irradiance in LEO.

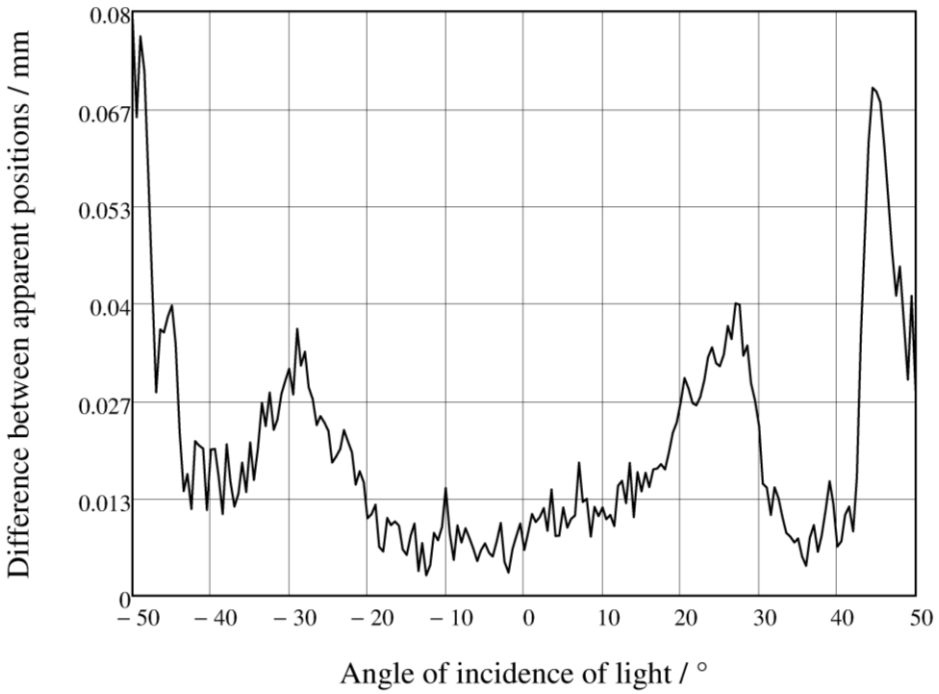

Figure 26. Difference between maximum and minimum values of apparent positions.

6.3.3 Uncertainty evaluation

The evaluation process of finding the contribution from irradiance uncertainty to the uncertainty of position measurements is structurally the same as for finding the thermal contribution to the uncertainty of position.

The difference between maximum and minimum value of irradiance is taken into account as type B source of uncertainty. Difference between maximum and minimum value of irradiance is

$$\Delta_I = 800 \frac{\mathrm{W}}{\mathrm{m}^2}. \tag{6.26}$$

The difference between maximum and minimum value of position in respective range of irradiance is

$$\Delta_{PI} = 0.04\,\mathrm{mm}. \tag{6.27}$$

Uncertainty of measured position due to irradiance is

$$u_{PI} = \frac{\Delta_{PI}}{\sqrt{12}} = 0.012\,\mathrm{mm}. \tag{6.28}$$

Converted into degrees:

$$u_I = u_{PI} \cdot PTA = 0.25°. \tag{6.29}$$

6.4 Tests in vacuum

Tests in vacuum indicate if vacuum causes permanent damages to the Sun sensors. An AR test is performed before putting the sensor in vacuum with pressure of 26(5) Pa for 0.5 hours and the same test is performed after taking the sensor from vacuum. Due to lack of necessary equipment, no tests were performed in vacuum conditions.

6.4.1 Testing process and results

The testing process was following:

1. The AR test was carried out,
2. The Sun sensor was placed into the vacuum chamber,
3. The sensor was kept in the chamber for 30 min at 26(5) Pa,
4. The sensor was taken out from the vacuum chamber,
5. The AR test was carried out.

Results indicate that there are no permanent damages when before and after test results are compared, yet there is no information about sensors performance in vacuum. Figure 27 shows

the difference between measured positions of before and after tests and it can be seen, that the differences are bound within the limit of precision of AR testing equipment and therefore the vacuum does not contribute to the uncertainty of Sun sensor measurements.

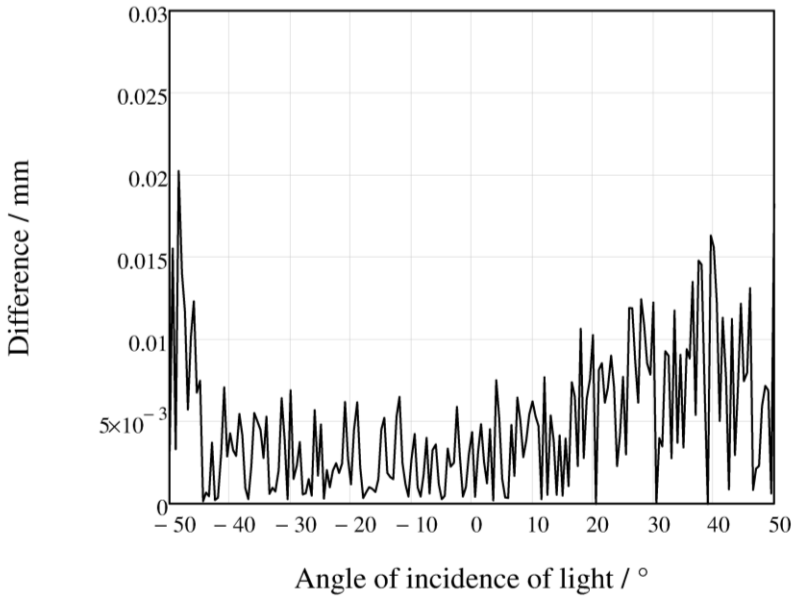

Figure 27. Difference between measured positions of before and after AR tests.

6.5 Effect of ultraviolet radiation on the Sun sensors

Ultraviolet radiation is high energy light that has sterilizing effects and produces photo-catalytic reactions [39]. On the other hand, UV radiation may induce degradation of thermo-optical properties, leading to decreased efficiency of the thermal control surfaces and strongly affecting mechanical properties [40]. The total energy provided by solar UV radiation in the range of 100 nm to 400 nm is about 8% of the solar constant [9].

The coating of S3931 PSD absorbs the wavelengths below 300 nm and therefore protects the sensor from UV radiation in the respective range of wavelengths of incident light [23, 42]. Also the resin coating, which is used on S3931, does not respond to UV radiation and therefore it was assumed, that the UV radiation causes potentially no deteriorations [23, 42]. Ordinary silicone PSDs have a problem of UV light reacting with protective resin coating of the PSD, which causes slow release of gas from the material and cause deterioration [41].

6.6 Calibration of ESTCube-1 Sun sensors

As a direct result from the tests, it can be seen in Figure 17 that when only measured data and masks geometrical properties are used to calculate the angle of Sunlight, the final angular output error builds up due to the deviations from the expected results, which are given by the model for AR tests. Thus interpolation functions are used for calculating the angle of incidence. Interpolation functions are formed from AR test data that links the measured position of light with ground calibrated angular value.

Each sensor was calibrated two times, having different light source per each calibration. Since a lamp with similar spectrum of Sun was not available, it was considered to use separate lamps, where one lamp (Halogen) had its spectrum shifted to infrared (IR) region and the other (Xenon) in UV region. The results of two calibrations were compared and ultimately average values between two separate calibrations were used for regressing calibration functions.

The calibration process with data analysis was following:

1. The AR test was carried out with lamp 1,
2. The AR test was carried out with lamp 2,
3. Average values were calculated between the results of two AR tests,
4. The boundaries of the FOV were determined,
5. The averaged results between the boundaries of the FOV were used in polynomial regression,
6. A calibration function was regressed.

Best fitting calibration functions were achieved by 10th order polynomial regression. Figure 30 shows an output of calibration measurements and a 10th order function regressed from the data. Compared to other AR figures, the angle of incidence and measured position on sensor are presented on opposite axes since the argument of the calibration function is position and the outcome of the function is angle of incidence of light.

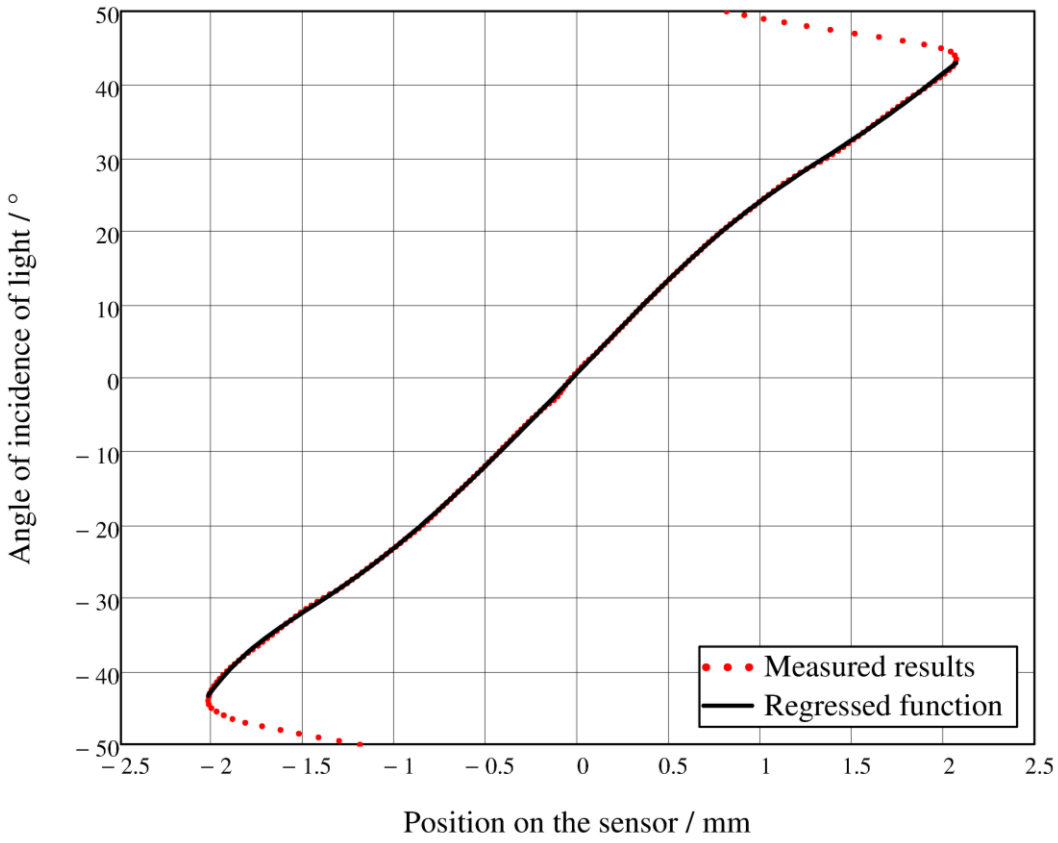

Figure 28. Output of calibration measurements and a 10th order function regressed from the data.

6.7 Uncertainty budget

The uncertainty components of the measurements of the Sun sensor, which were obtained from test results and datasheets, are presented in Table 5 where the presented quantities are following:

δP_T - Temperature drift,

δP_I - Solar irradiance uncertainty,

δP_P - Precision of setting up the angle test equipment,

δR - Rotation bench's precision,

δP_S - Repeatability of single angular measurement during calibration,

δP_{LSB} - LSB influence on ADC measurements,

Table 5. Uncertainty budget.

Quantity	**Estimate**	**Standard uncertainty**	**probability distribution**	**sensitivity coefficient**	**Uncertainty contribution in °**
δP_T	(−9…75) °C	0.035 mm†	Rectangular	21.6 °/mm	0.76
δP_I	(1000… 1800) W/m^2	0.012 mm†	Rectangular	21.6 °/mm	0.25
δP_P	0 mm	0.004 mm	Normal	21.6 °/mm	0.08
δR	0.005°	1.44° 10^{-3}	Rectangular	1	0.001
δP_S	0 mm	$1.7 \cdot 10^{-4}$ mm	Normal	21.6 °/mm	0.005
δP_{LSB}	0 LSB	1 LSB / $\sqrt{12}$	Rectangular	0.056 °/mm	0.02
Sum (root mean square) 95% confidence level, k = 2	---	---	---	---	**1.6°**

The estimated expanded uncertainty of Sun sensor angular measurements is 1.6°. The expanded uncertainty of angular measurement is stated as the standard uncertainty of measurement multiplied by the coverage factor $k = 2$, which for a normal distribution corresponds to a coverage probability of approximately 95%. The estimated value uncertainty satisfies the requirement for estimating the angle of incidence of Sunlight with accuracy better than 3° per axis.

6.8 Influence from Earth's albedo

Albedo is a coefficient that shows the relation between incident amount of light and the amount that reflects back from Earth. The average value of Earth's albedo is about 30% while in Polar regions it can be as high as 90% [38]. Based on data provided by a project of NASA called "Total Ozone Mapping Spectrometer" (TOMS) and albedo modeling that used the data of TOMS, it can be estimated where the influence of albedo is the highest, depending on Earth's longitude and latitude [36, 37]. As the light reflected by Earth is emitted diffusely, the model

† Standard uncertainty of position measurements caused by respective source of uncertainty.

implements Lambertian cosine law to calculate the light received by the satellite in any position above the Earth's surface in LEO.

6.8.1 Uncertainty estimation

Due to limited FOV of the Sun sensor, there are some latitude and longitude regions where albedo should have negligible influence on the measurements of the Sun sensor. These non-albedo influenced (NAI) regions can be seen in Figure 28. The angle *a*, which is measured between Sun vector and a line connecting the satellite and the center of Earth, indicates the limits of NAI region. That is because in Sun angle estimation, the most illuminated Sun sensor is used in calculations. The satellite is situated in LEO, with average height from ground being 650 km [4]. The radius of Earth is approximately 6371 km [9]. Knowing the orbit of the satellite and the radius of Earth, the relative regions of latitude and longitude, where albedo has no influence, are

$$a = a\cos\left(\frac{R}{R+LEO}\right) = \pm 24° \tag{6.30}$$

where *R* is the radius of Earth, *LEO* is the height of Low-Earth orbit.

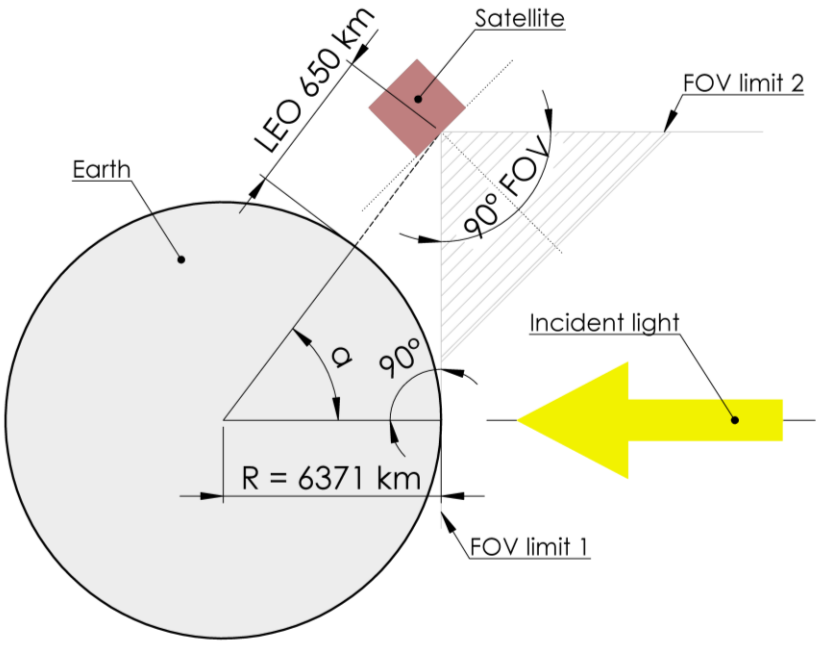

Figure 29. When the angle *a* is smaller than ±24°, Earth's albedo has no influence on Sun sensor measurements.

The influence of albedo on sensor measurements starts to increase when NAI region is exceeded. According to the model of Earth's albedo, the most influential region is in 60° latitude. In latitude of 90° to 70° albedo has negligible effect. Depending on the FOV of the Sun sensor, latitude and orientation of the satellite, the measurement error caused by albedo can be estimated. Figure 29 shows the measurement error that is caused by albedo in 60° latitude. In this estimation, the satellite is assumed to spin and the spin is expressed in change of angle of incidence of Sunlight.

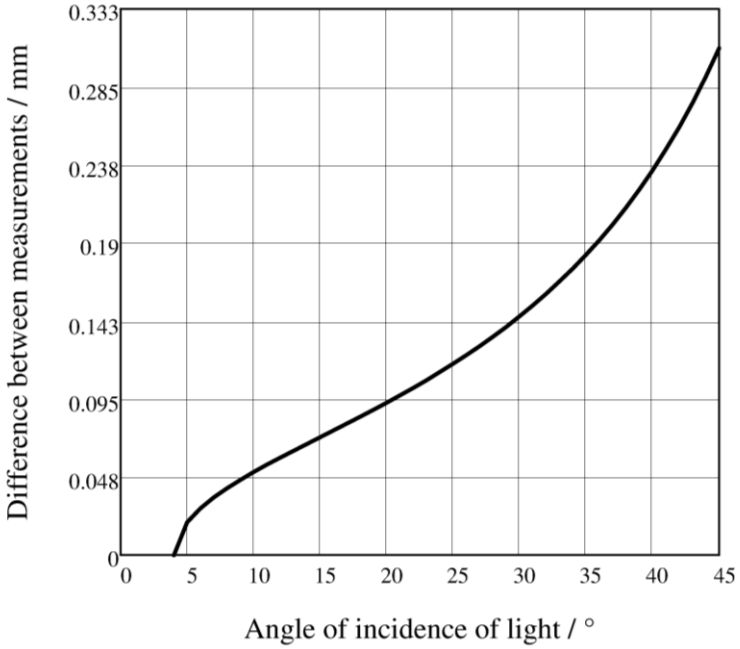

Figure 30. Difference between non albedo influenced and influenced Sun sensor measurements depending on angle of incidence of Sunlight.

The maximum influence of albedo is taken into account as a source of type B uncertainty of measured position. Since in NAI region and polar areas (further called NAI regions) the effect of albedo is negligible, approximately half of the period when the satellite is not in eclipse, albedo has no effect on sensor measurements. When assuming rectangular probability distribution, where the measurement uncertainty is distributed evenly within the approximate measurement range of ±90° latitude, the NAI regions must be taken into account. Therefore when maximum difference between NAI and influenced measurements is

$$\Delta_{Albedo} = 0.31\,\text{mm}\,. \tag{6.31}$$

The type B uncertainty of Sun sensor measurements caused by Earth's albedo is

$$u_{Albedo} = \frac{\Delta_{Albedo}}{2\sqrt{12}} = 0.045\,\text{mm}\,. \tag{6.32}$$

Converted into degrees:

$$u_{Albed} \cdot PTA = 1^\circ\,. \tag{6.33}$$

The estimated influence of Earth's albedo results an additional contribution to uncertainty of the measurements of the Sun sensor in LEO. Therefore the net uncertainty of the measurements of the sensor is **2.5**° with coverage probability of approximately 95%.

7 Conclusions

Sun sensors were developed to be used on ESTCube-1 satellite. The developed devices are analog sensors, utilizing Hamamatsu S3931 PSDs which detect the position of incident light on the PSD.

The sensor weighs 4.6 g, has dimensions, together with electronics board, of 21 mm × 24 mm × 3.7 mm and consumes on average 16 mW of power with peak consumption of 30 mW. The FOV of the sensor is ~90°.

Sun sensors were tested to estimate endurance and measurement uncertainty in LEO conditions and 6 sensors were calibrated and implemented on ESTCube-1. The sensors were required to withstand temperatures in expected temperature range is from −30 ºC to +40 ºC, operate at solar irradiance level of 1366 W/m^2 and withstand Ultraviolet (UV) radiation in the wavelength range of 100 nm to 400 nm at least for 1 year without malfunctioning. The most important findings of this work are following:

- The accuracy of measuring the angle of incidence of light with the developed Sun sensor is 2.5° and the device is suitable for coarse estimation of Sun's direction in LEO.
- Earth's albedo and temperature are the most influential contributors to uncertainty of measurements of the Sun sensor.
- The sensor fulfills the requirements for withstanding the conditions confronted in LEO.
- The proposed and developed Sun sensor is suitable for ESTCube-1 mission.

The future perspectives for the Sun sensor are to develop a model that can reduce influence of the major contributors to the uncertainty of the measurements of the Sun sensors and to optimize the design even further thereby achieving greater value of the FOV and better accuracy.

8 Summary

ESTCube-1 is Estonia's first satellite that is developed mainly by the students of Tartu University. The main objective of the project is to test the electric solar wind sail propulsion concept, proposed by Pekka Janhunen.

An essential part of the mission is determining and controlling the attitude of the satellite, which is a task of respective module of the satellite that performs detumbling, pointing and spin control of the satellite. The attitude determination system uses three-axis magnetometers, three-axis qyroscopes and two-axis Sun sensors to gather information about the orientation of the satellite in space. While commercial off-the-shelf components were used for magnetometers and qyroscopes, Sun sensors were custom-built based on analog one-dimensional position sensitive detectors.

The main goals of this work were to optimize, test and calibrate the Sun sensors for ESTCube-1 and to evaluate the uncertainty for the measurements of the developed Sun sensor. During a period of one year the proposed concept for Sun sensor was theoretically analyzed, optimized, and tested by the author to meet requirements of the mission. As a result of the work, a low-power, lightweight device was developed that meets requirements of ESTCube-1 mission, fulfilling all the goals defined for this thesis.

9 Acknowledgements

I would like to thank my supervisors Andris Slavinskis and Riho Vendt for giving excellent advices throughout the work. Also I would like to express my gratitude to Ilmar Ansko and Viljo Allik for providing testing equipment and theoretical knowledge.

Thanks to Erik Kulu, Hendrik Ehrpais, Jaan Viru and Tõnis Eenmäe for contributing to my work by sharing ideas and solutions, especially Erik Kulu for proposing the concept of developed Sun sensor and realizing the design of the Sun sensor's mask .

Kokkuvõte

ESTCube-1 Päikeseandurite karakteriseerimine

ESTCube-1 on Tartu Ülikoolis peamiselt tudengite poolt arendatud satelliit, mille põhieesmärgiks on katsetada Soome Meteoroloogia Instituudi professori, Pekka Janhuneni, poolt väljatöötatud elektrilist päikesepurje.

Missiooni läbiviimise seisukohalt on oluline teada ja kontrollida satelliidi asendit, olles vastavalt tehiskaaslase pardal asuva asendi määramise ja kontrollimise mooduli ülesandeks, mis viib läbi satelliidi pöörlemiskiiruse muutmise ja suunamise. ESTCube-1 asendi määramise süsteem kasutab satelliidi orientatsiooni hindamiseks kolmeteljelisi magnetomeetreid, kolmeteljelisi güroskoope ning kaheteljelisi päikeseandureid. Erinevalt güroskoopidest ja magnetomeetritest, mis on kaubanduslikult kättesaadavad, disainiti ja valmistati päikeseandurid koha peal.

Käesoleva töö eemärgiks oli analüüsida, optimeerida, testida ning kalibreerida väljapakutud päikeseanduri disaini, tagamaks anduri vastupidavuse maalähedase orbiidi tingimustes ning täitmaks tehiskaaslase missioonist tulenevaid nõudeid. Aasta pikkuse töö tulemusena töötati välja kerge, väikese võimsustarbega ning ESTCube-1 nõuetele igati vastav päikeseandur, täites kõik eesmärgid, mis sai antud töö jaoks püstitatud.

References

[1] "Estonian student satellite project," http://www.estcube.eu/ (accessed 11 May 2013).

[2] "CubeSat Design Specification Rev. 12," California State Polytechnic University (2009). http://www.cubesat.org/images/developers/cds_rev12.pdf (accessed 11 May 2013).

[3] P. Janhunen, "Electric Sail for Producing Spacecraft Propulsion," U.S. Patent No. 7,641,151 (2006).

[4] Janhunen, P., P.K. Toivanen, J. Polkko, S. Merikallio, P. Salminen, E. Haeggström, H. Seppänen, R. Kurppa, J. Ukkonen, S. Kiprich, G. Thornell, H. Kratz, L. Richter, O. Krömer, R. Rosta, M. Noorma, J. Envall, S. Lätt, G. Mengali, A.A. Quarta, H. Koivisto, O. Tarvainen, T. Kalvas, J. Kauppinen, A. Nuottajärvi and A. Obraztsov, "electric solar wind sail: Towards test missions (Invited article)", Rev. Sci. Instrum., 81, 111301, 2010.

[5] J. R. Wertz, ed., *Spacecraft Attitute Determination and Control* (Kluwer Academic Publishers, 1990).

[6] M. Griffin and J. French, *Space Vehicle Design* (American Institute of Aeronautics and Astronautics, 2004).

[7] G. Rufino and M. Grassi, "Multi-Aperture CMOS Sun Sensor for Microsatellite Attitude Determination," MDPI, **9**, 4503-4524 (2009).

[8] A.Scholz, W. Ley, B. Dachwald, J.J. Miau, "Fligh Results of the COMPASS-1 Picosatellite Mission," Acta Astronautica, **67**, 1289-1298 (2010).

[9] P. V. Foukal, *Solar Astrophysics* (John Wiley & Sons, 2008).

[10] "DTUsat project page," http://dtusat.dtu.dk/ (accessed 11 May 2013).

[11] H. P. Contesse, “Phase B/C Report of SwissCube ADCS System and Hardware,” Tech. Rep., Federal Polytechnic of Lausanne (2007). http://ctsgepc7.epfl.ch/06%20-%20Attitude%20control/S3-B-C-ADCS-1-3-ADCS_HW_and_System.pdf (accessed 11 May 2013).

[12] J. Gießelmann, “Development of an Active Magnetic Attitude Determination and Control System for Picosatellites on highly inclined circular Low Earth Orbits,” Master’s thesis, Royal Melbourne Institute of Technology (2006).

[13] M. Pedersen, J. H. Hales, ”Linear Two-Axis MOEMS Sun Sensor,” Tech. Rep., Technical University of Denmark (2004). http://hvig.dk/files/Pedersen-and-Hales-2004-Linear-Two-Axis-MOEMS-Sun-Sensor-Technical-Report.pdf (accessed 11 May 2013).

[14] A. Scholz, J. J. Miau, J. C. Juang, “PACE - Taiwans’s First Nanosatellite for Evaluation of Momentum-Biased Attitude Control,” National Cheng Kung University (2004). http://satellite.ncku.edu.tw/pace/download/IAA-B7-0703_paper.pdf (accessed 11 May 2013).

[15] A. Scholz, J. J. Miau, J. C. Juang, C. C. Ker , B. C. Chen, H. L. Chiu, J. T. Tu, “Design and Development of Digital CMOS Sun Sensors for Precise Attitude Determination of Small Satellites,” Tech. rep., National Cheng Kung University (2007). http://satellite.ncku.edu.tw/pace/download/UNIVERSAT_2007_paper.pdf (accessed 11 May 2013).

[16] L. Alminde, M. Bisgaard, D. Vinther, T. Viscor, K. 0stergard, "Educational value and lessons learned from the AAU-CubeSat project," Proceedings of International Conference on Recent Advances in Space Technologies, 57-62 (2003).

[17] K. Krogh, E. Schreder, “Attitude Determination for AAU CubeSat,” Tech. rep., Alborg University (2002). http://www.space.aau.dk/cubesat/dokumenter/ADC-report.pdf (accessed 11 May 2013).

[18] A.A. Vaartjes, W.J. Ubbels, R.J. Hamann, “The Delfi-C3 Student Nanosatellite,” Proceedings of the AMSAT-UK Colloquium, Surrey, United Kingdom (2005).

[19] E. Boslooper, N. Heiden, D. Naron, R. Schmits, J. J. Velde, J. Wakeren, "BepiColombo Fine Sun Sensor," Tech. rep., Netherlands Organization for Applied Scientific Research (2012). http://congrex.nl/icso/2012/papers/FP_ICSO-029.pdf (accessed 11 May 2013).

[20] W.J. Ubbels, A.K. Bonnema, k.D. Breukelen, J.H. Doom, R. van den Eikhofql, E. Van der Linden, G.T. Aalbers, J. Rotteveel, R.J. Hmann, C.J.M. Verhoeven, "Delfi-C3: a Student Nanosatellite As a Test-Bed for Thin Film Solar Cells and Wireless Onboard Communication," Proceedings of 2nd International Conference on Recent Advances in Space Technologies, 167-172 (2005).

[21] "Homepage of CubeSatShop," http://www.cubesatshop.com/ (accessed 11 May 2013).

[22] CubeSatShop Sun sensor, "CubeSat Sun Sensor," http://www.cubesatshop.com/index.php?page=shop.product_details&flypage=flypage.tpl&product_id=104&category_id=7&option=com_virtuemart&Itemid=69 (accessed 11 May 2013).

[23] Hamamatsu, "Position Sensitive Device S3931," http://www.hamamatsu.com/resources/pdf/ssd/s3931_etc_kpsd1002e06.pdf (accessed 11 May 2013).

[24] Hamamatsu, "Position Sensitive Device S3932," http://www.hamamatsu.com/resources/pdf/ssd/s3931_etc_kpsd1002e06.pdf (accessed 11 May 2013).

[25] Hamamatsu, "Position Sensitive Device S2044," http://www.hamamatsu.com/resources/pdf/ssd/s1880_s2044_kpsd1015e06.pdf (accessed 11 May 2013).

[26] Hamamatsu, "Position Sensitive Device S5990," http://www.hamamatsu.com/resources/pdf/ssd/s5990-01_etc_kpsd1010e04.pdf (accessed 11 May 2013).

[27] Hamamatsu, “Position Sensitive Device S5991,” http://www.hamamatsu.com/resources/pdf/ssd/s5990-01_etc_kpsd1010e04.pdf (accessed 11 May 2013).

[28] Maxim Integrated, “Analog-to-Digital Converter MAX 1230,” http://datasheets.maximintegrated.com/en/ds/MAX1226-MAX1230.pdf (accessed 11 May 2013).

[29] Texas Instruments, “Operational Amplifier OPA 3433,” http://www.ti.com/general/docs/lit/getliterature.tsp?genericPartNumber=opa4344&fileType=pdf (accessed 11 May 2013).

[30] Texas Instruments, “Low-Dropout Regulator LP2985aim 5-4.5,” http://www.ti.com/lit/ds/symlink/lp2985-n.pdf (accessed 11 May 2013).

[31] Motorized Rotation Stage, “MOR-100,” http://www.optics-focus.com/motorized-rotation-stage-p-523.html (accessed 17 May 2013).

[32] 3-axis Motion Controller,”MOC-3,” http://www.optics-focus.com/motion-controller-p-544.html (accessed 17 May 2013).

[33] National Instruments, “LabVIEW,” http://www.ni.com/labview/release-archive/2011/ (accessed 11 May 2013).

[34] Lab Jack, “Data Acquisition Device UE9,” http://labjack.com/printpdf/book/export/html/192 (accessed 11 May 2013).

[35] Heraeus Votch, “Thermal chamber VMT 04/16,” Thermal Test Chamber nr 45383.

[36] “Total Ozone Mapping Spectrometer,” http://ozoneaq.gsfc.nasa.gov/ (accessed 11 May 2013).

[37] S. Theil, P. Appel, A. Schleicher, “Low Cost, Good Accuracy - Attitude DeterminationUsing Magnetometer and Simple Sun Sensor,” Small Satellite Conference (2003).

[38] R. B. Stull, *Meteorology for Scientists and Engineers* (Brooks/Cole Pub Co, 1999).

[39] B. Neppolian, H.C. Choi, S. Sakthivel, Banumathi Arabindoo, V. Murugesan, "Solar/UV-Induced Photocatalytic Degradation of Three Commercial Textile Dyes," Journal of Hazardous Materials, **89**, 303-317 (2002).

[40] E. Grossman, I. Gouzman, "Space Environment Effects On Polymers In Low Earth Orbit," Nuclear Instruments and Methods in Physics Research Section B: Beam Interactions with Materials and Atoms, **208**, 48-57 (2003).

[41] Y.Q. Li, Y. Yang, S.Y. Fu, "Photo-Stabilization Properties of Transparent Inorganic UV-Filter/Epoxy Nanocomposites," Composites Science and Technology, **67**, 3465-3471 (2007).

[42] Hamamatsu, "Handbook of Si Photodiode," Tech. Rep., http://www.hamamatsu.com/resources/pdf/ssd/e02_handbook_si_photodiode.pdf (accessed 15 May 2013).

[43] Philips Semiconductors, "Temperature sensor KTY82-1," http://www.nxp.com/documents/data_sheet/KTY82_SER.pdf (accessed 21 May 2013).

Lihtlitsents lõputöö reprodutseerimiseks ja lõputöö üldsusele kättesaadavaks tegemiseks

Mina Robert Valner

(sünnikuupäev: 21.01.1991)

1. annan Tartu Ülikoolile tasuta loa (lihtlitsentsi) enda loodud teose

„Characterization of Custom Built Sun Sensors For ESTCube-1“

mille juhendajad on Riho Vendt ja Andris Slavinskis

1.1. reprodutseerimiseks säilitamise ja üldsusele kättesaadavaks tegemise eesmärgil, sealhulgas digitaalarhiivi DSpace-is lisamise eesmärgil kuni autoriõiguse kehtivuse tähtaja lõppemiseni;

1.2. üldsusele kättesaadavaks tegemiseks Tartu Ülikooli veebikeskkonna kaudu, sealhulgas digitaalarhiivi DSpace´i kaudu kuni autoriõiguse kehtivuse tähtaja lõppemiseni.

2. olen teadlik, et punktis 1 nimetatud õigused jäävad alles ka autorile.

3. kinnitan, et lihtlitsentsi andmisega ei rikuta teiste isikute intellektuaalomandi ega isikuandmete kaitse seadusest tulenevaid õigusi.

Tartus **27.05.2013**